UNIVERSIDADE D
COIMBRA

Hugo Emanuel Costa Vidinha

NUMERICAL EVALUATION OF THE EFFECTS OF SEAWATER ON THE STRENGTH OF GLASS FIBER REINFORCED POLYMERS

Masters Dissertation in Mechanical Engineering in the speciality of Energy and Environment

July 2022

1 2  9 0

FACULDADE DE CIÊNCIAS E TECNOLOGIA
UNIVERSIDADE D COIMBRA

NUMERICAL EVALUATION OF THE EFFECTS OF SEAWATER ON THE STRENGTH OF GLASS FIBER REINFORCED POLYMERS

A dissertation submitted in partial fulfilment of the requirements for the degree of Master in Mechanical Engineering in the speciality of Energy and Environment

Avaliação Numérica da Resistência Mecânica de Compósitos Imersos em Água Salgada

Author

Hugo Emanuel Costa Vidinha

Advisors

Professor Maria Augusta Neto

Professor Ricardo Nuno Madeira Soares Branco

Committee

Chair	**Professora Doutora Ana Paula Bettencourt Martins Amaro** **Professor Auxiliar com Agregação da Universidade de Coimbra**
Members	**Professor Doutor Paulo Nobre Balbis dos Reis** **Professor Associado da Universidade de Coimbra** **Professor Doutor Ricardo Nuno Madeira Soares Branco** **Professor Auxiliar da Universidade de Coimbra**

Coimbra, Julho, 2022

Success is the natural consequence of consistently applying basic fundamentals.

-James Rohn

Agradecimentos

O desenvolvimento deste trabalho só foi possível graças ao contributo e apoio de algumas pessoas, às quais não posso deixar de prestar o meu reconhecimento.

Em primeiro lugar, gostaria de expressar o meu agradecimento aos meus orientadores, Sra. Professora Doutora Maria Augusta Neto e Sr. Professor Doutor Ricardo Nuno Madeira Soares Branco, que me deram força, mesmo nas piores horas. Um muito obrigado por toda a motivação, orientação, disponibilidade e simpatia.

Aos meus pais e irmão, por toda educação, apoio, persistência, compreensão e pela oportunidade de concluir este ciclo. Sem eles não seria possível. Por isto e por tudo o que já fizeram por mim, estarei eternamente grato.

À Paula pelo incentivo, compreensão, pelo apoio ao longo destes anos e por estar presente nos bons momentos e especialmente nos menos bons. O meu muito obrigado.

Ao Cristian, Andreas, Afonso, Figueira e ao Diogo pela amizade, cumplicidade, por todos os momentos bem passados, e por tornarem o meu percurso académico numa jornada tão positiva. A cada um de vocês, um enorme obrigado.

Aos meus avós, por todo o carinho e educação.

Aos meus padrinhos por toda a ajuda e por acreditarem sempre em mim.

A todos, um bem-haja.

Abstract

The employment of composite materials in the marine industry has been gradually considered due to their enhanced mechanical properties and good corrosion resistance. However, their cost in marine structures is not the lowest as a consequence of the current conservative structural safety factors. Establishing an accurate numerical model for predicting the long-term behavior of composites in the marine environment could be a valuable tool since it would reduce structural costs by reducing safety factors.

Therefore, the presented work's main objective is to develop a numerical model to predict the behavior of glass fiber-reinforced polymers exposed to the marine environment.

In this work, Puck's failure criterion is first applied, a failure theory for unidirectional fiber-reinforced polymer composites, which has proven its capability in multiple stress states by many researchers. Then, Fick's first diffusion law was used to predict the seawater absorption rate. Finally, a relation between Fick's law and the diffusion distance was assumed to predict the seawater concentration in the specimen. The developed model main's methodology is to adapt the lamina's material properties as a function of the seawater concentration in the structure.

The model was implemented within an implicit Finite Element Analysis (FEA) in the commercially available FEA software supported by a subroutine developed in Fortran 95.

The model was validated with tensile strength tests using specimens not immersed and immersed for 900 days in seawater. The model agreed well with the experimental data regarding the failure load and displacement at failure. It was also predicted the most critical surfaces to protect from hostile environments.

Keywords: Glass Fiber-reinforced polymers, Puck's failure criterion, Seawater degradation, Fick's law.

Resumo

O uso de materiais compósitos na indústria naval tem sido cada vez mais considerado devido às suas aprimoradas características mecânicas e à sua boa resistência à corrosão. No entanto, o seu custo em estruturas marítimas não é o mais baixo em consequência dos atuais, conservadores, fatores de segurança. A criação de um modelo numérico preciso, capaz de prever o comportamento, a longo prazo, de compósitos em ambiente marinho poderá ser uma ferramenta valiosa, pois poderá reduzir os custos das estruturas reduzindo os seus fatores de segurança.

Com isto, o principal objetivo do trabalho apresentado é desenvolver um modelo numérico para prever o comportamento de polímeros reforçados com fibra de vidro expostos ao ambiente marinho.

Neste trabalho, primeiramente, foi utilizado o critério de falha de Puck, uma teoria de falha para compósitos unidirecionais reforçados com fibra, que provou a sua fiabilidade em múltiplos estados de tensão, por vários investigadores. Seguidamente, a primeira lei de Fick para a difusão foi utilizada para prever a taxa de absorção da água do mar. Por último, uma relação entre a lei de Fick e a distância de difusão foi assumida para prever a concentração de água do mar no provete. A principal metodologia de funcionamento do modelo desenvolvido é adaptar as propriedades das lâminas em função da concentração de água do mar na estrutura.

Este modelo foi implementado numa análise implícita de elementos finitos implementada num programa comercial de elementos finitos, através de um sub-rotina escrita em Fortran 95.

O modelo foi validado com resultados de ensaios de resistência à tração executados com corpos de prova não imersos e imersos 900 dias em água salgada. O modelo apresentou resultados coerentes com os dados experimentais no que diz respeito à carga máxima e deslocamento na falha. Através do modelo, foi ainda possível prever, as superfícies críticas a proteger de ambientes hostis.

Palavras-chave: Compósito reforçados com fibra de vidro, Critério de falha de Puck, Degradação pela água do mar, Lei de Fick.

Contents

LIST OF FIGURES

LIST OF TABLES

NOTATION

Coordinate systems

x, y, z	Global coordinate system
x_1, x_2, x_3	Coordinate system of a UD lamina
x_1, x_n, x_t	Coordinate system of the action plane
$x_\perp, x_\parallel$	Cylindrical coordinate system of a UD lamina

List of Symbols

ε	Normal strain
θ	Angle of the action plane
v	Poisson's ratio
σ	Normal stress
ψ	Angle of the resultant shear in the action plane
δ	Displacement
τ	Shear stress
c	Index denoting compression
C	Seawater concentration
c_d	Dilatational wave speed
C_{ij}^0	Initial material stiffness tensor
C_{ij}	Damaged material stiffness tensor

C_{CS}	Element's seawater concentration relative to its closer permeable surface
d	Damage parameter
D_{Coef}	Diffusion coefficient
D_{CS}	Element's axis distance to its closer permeable surface
$D_{i\ distOrigin}$	Normal axis distance to origin of the surface
E	Young's modulus
f	Index denoting fiber
f_e	Stress exposure
fp	Index denoting fracture plane
G	Shear modulus
GP	Gauss point
h	Thickness
ID	Immersion days
k	Experimental curve fitting parameter
L	Load
L_{min}	Smallest element dimension in the mesh
m	Index denoting matrix
M_t	Moisture absorption contend
M_∞	Maximum amount moisture of absorption
m_{σ_f}	Magnification factor due to Poisson's effect
N_{Fl}	Normalized Fick's law
p	Inclination parameter
R^A	Fracture resistance of the action plane
s_{mt}	Loss control factor
W_{volume}	Specimen's volume affected by the seawater diffusion
$\parallel$	Index denoting the direction parallel to the fiber
$\perp$	Index denoting the direction perpendicular to the fiber

Acronyms

2D	Two-dimensional
3D	Three-dimensional
DIC	Digital image correlation
DOF	Degrees of freedom
ESL	Equivalent single layer
FE	Finite element
FEA	Finite element analysis
FRP	Fiber reinforced polymers
IFF	Inter fiber fracture
LW	Layer-Wise
MFB	Master fracture body
UMAT	User material subroutine

1. INTRODUCTION

Composite materials, especially fiber-reinforced polymers (FRP), possess very attractive physical and mechanical properties, such as high specific stiffness and strength, relative to traditional materials. This is reflected in the growth of their use in areas where light, strong structures are required, for example, in the aerospace and automobile industries. These enhanced mechanical properties make them reliable substitutes for metals [1]. Also, due to their high corrosion resistance, FRPs have aroused great interest in marine applications. Meanwhile, using composite materials in hostile environments can significantly modify their mechanical behavior. **Figure 1.1.** shows the share of total value of composites and how the marine industry only represents 3% of the total share. That can be partially justified by the fact that the application of glass-fiber reinforced polymers (GFRPs) to the naval industry has often been accompanied by the application of conservative design safety factors [2].

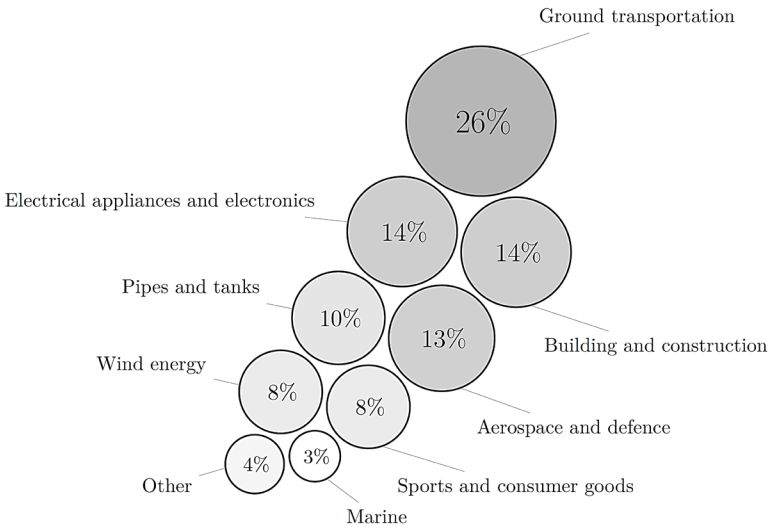

Figure 1.1. Share of total value of composites, from [3].

In marine sectors, composites have been used in traditional boats and ship structures. Fiber-reinforced polymers are also starting to provide key contributions in offshore industry and renewable marine energy [4]. Understanding the long-term behavior of composite

components in marine environment, is a great challenge, although, if achieved, it can largely expand the composite industry.

The cost of the marine structures can be significantly reduced by lowering the current conservative safety factors. To reduce those safety factors, it is necessary to understand what damage mechanisms lead to failure and how the environment modifies those damage mechanisms. Furthermore, creating an accurate numerical model capable of predicting the seawater effects and the failure of FRP with finite element analysis (FEA) can considerably reduce the costs by reducing safety factors.

A failure criterion must be used to model the failure of an FRP composite. The prediction of failure of fiber-reinforced composites, considering a specified state of stress, is extremely complex. From a microstructural point of view, the enormous amount of interactions between fiber and matrix would require the analytical detection of successive microstates of stress, representing an extremely expensive computationally task [5]. On the other hand, if a macro mechanics approach is considered using an accurate three-dimensional failure criterion, precise simulation results can be achieved using acceptable computational effort.

In the *"World Wide Failure Exercise"* (WWFE), an exercise where numerous composite failure theories were compared with experimental results, the Alfred Puck failure criterion has proven to be the one with superior characteristics [6]. Puck's failure criterion not just predicts failure, but it is also capable of distinguishing different fracture modes and predict the gradual failure process. It is important to mention that these failure criteria tested in the WWFE concentrate on monotonously increasing loads until the failure happens. Most structures, however, are stressed by alternating loads and fail because of the gradual increase in damage. Still, since it is hard to implement a reliable fatigue life model, Puck's failure criterion is a remarkable tool. Therefore, Puck's failure criterion will be implemented in this work to predict failure.

1.1. Objectives

The primary purpose of this thesis is to develop and implement a numerical model capable of predicting the hostile environment effects on the strength and the mechanical behavior of glass fiber-reinforced polymers (GFRP). The hostile environment in study is seawater. The numerical model will be validated with experimental tensile test results obtained for specimens not immersed and immersed for 900 days in seawater. The final model resulting from the association of Puck's failure criterion and the model to be developed must be able to:

- Predict the load and displacement at failure as a function of the immersion days;
- Predict matrix and fiber damage patterns;
- Predict the behavior of the material as a function of the immersion days.

A series of steps must be carried out to fully develop the numerical model. The first stage is the literature review. In this step, all the theory used in the development of the model is presented, including:

- Types of damage on composites;
- Representation of composites in FEA software;
- Puck's failure criterion;
- Lamina's constitutive relation;
- Finite analysis method;
- Seawater effects on the properties of composites.

Then, in the development phase, the following steps must be accomplished:

- Model the composite and the test conditions in the FEA software;
- Develop the numerical model;
- Implement the numerical model.

It is essential to mention that the complexity of composite structures forces the scope of this work to be limited to:

- Fiber-reinforced polymers;
- Quasi-static loading. Fatigue or time-dependent methods are not covered;

- The seawater effects. The exposure effects of other environments are not debated.

1.2. Dissertation structure

With the purpose of helping the reader, this section presents the structure of the dissertation, which is divided into five chapters organized as follows:

Chapter 1 – This first chapter contains an introductory review of composites and their current position in marine applications. It also introduces the failure criteria to be implemented and defines the objectives for the present work.

Chapter 2 – Chapter two presents all the theory used to develop the model. Initially, it presents the types of damage in composites, which is essential to later understand the failure criterion. Then introduces the procedure to represent a laminate in FEA software. Next, the failure criterion, the FEA method, and the lamina's constitutive relation are described. Lastly, a summary of previous research conducted to understand the seawater effects in composites is presented.

Chapter 3 – The third chapter explains the methodologies used to develop the numerical model from the development of the model to its implementation in a user material subroutine environment. It also shows the experimental results obtained previously in other studies.

Chapter 4 – In the fourth chapter, the numerical model results are presented, discussed, and compared with the experimental.

Chapter 5 – Conclusions and recommendations for future works are summarized in the fifth chapter.

2. STATE OF THE ART REVIEW

2.1. Composites

Composites can be defined as materials with two or more constituents of different phases that cannot be combined chemically into one single-phase material. One of the constituents is the reinforcement phase, a discontinuous phase with higher strength and stiffness. The other phase is the matrix, a continuous phase that binds the reinforcements together. The combination of these constituents forms a new material with enhanced properties.

There are numerous types of composites based on the shape of the reinforcements, but the relevant one for this study is the Fiber-Reinforced Polymer. Fiber-Reinforced Polymer materials are constituted of strong fibers inserted in a resin matrix. The fibers provide strength and stiffness to the composite and carry most applied loads. The matrix acts to bond and protect the fibers and transfers stress from fiber to fiber through shear stresses.

2.2. Damage and failure of laminates

Failure is the inability of a given system to perform its design function. Fracture is one example of a possible failure, but generally, a material can have a local fracture and still perform its design function. In composites, fiber breakage, cracks in the matrix, and fiber/matrix debonds are some types of fractures.

The damage is a collection of all the irreversible changes in a material brought about by a set of energy dissipating physical or chemical processes [7]. Examples of damage in composites are multiple fiber-bridged, matrix cracking, and local delamination.

The composite's anisotropy, which is formed by the heterogeneous microstructure of composites, the significant differences between constituent properties, and the presence of interfaces, are reasons for the composite’s micro-level forms of damage [7]. This anisotropy verified in fiber-reinforced composites induces highly complex and difficult to predict

damage behaviors. Therefore, this section will concisely explain some types of damage in FRP composites along with the two kinds of failure adopted in Puck's failure theory.

2.2.1. Micro-cracks.

Matrix microcracking is usually the first type of damage observed in a fiber-reinforced composites [8]. The type of micro-damage influences both, material's stiffness, and strength. One of the most critical moments for micro-cracks formation is after curing [9]. After curing, considerable residual stresses are generated in the matrix due to different thermal expansion coefficients. These stresses can lead to three types of small matrix cracks shown in **Figure 2.1** and local debonding of fiber and matrix shown in **Figure 2.2.** Further tiny cracks occur when the part is mechanically loaded for the first time. Both length and number of cracks grow if the stress level in the matrix is increased. In laminates with various plies, the microdamage formed in one ply can grow to traverse the thickness of that ply but never run to a different ply [7]. If micro-cracks develop to a certain point, a macroscopic crack is formed, which runs through the thickness of a layer. This macro-mechanical damage is named Inter Fiber Fracture (IFF) in Puck's terminology.

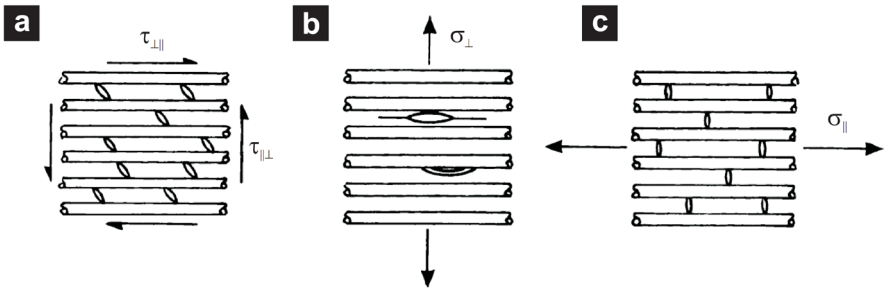

Figure 2.1. Micro-defects due to: (a) shear tension $\boldsymbol{\tau}_{\perp\parallel}$, (b) fiber-perpendicular tension $\boldsymbol{\sigma}_{\perp}$ and (c) fibre-parallel tension $\boldsymbol{\sigma}_{\parallel}$, from [10] .

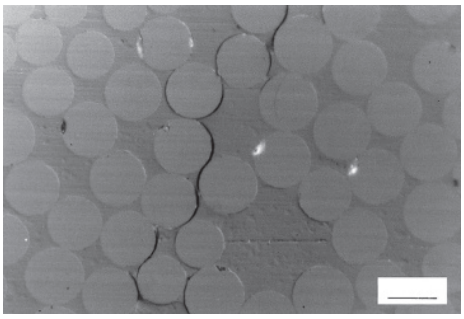

Figure 2.2. Debonds in a fiber-reinforced composite, from [11].

2.2.2. Inter fiber fracture (IFF)

Inter Fiber Fracture (IFF) is a terminology introduced by Alfred Puck and refers to a crack that runs parallel to the fibers through a layer's entire thickness [12]. An inter-fiber failure is very likely to happen when a lamina is loaded with a fiber-perpendicular or shear stress as shown in **Figure 2.4.** The cohesion between the broken and the neighboring layers is affected locally, but the laminate's integrity is still preserved. The presence of IFF leads to a redistribution of forces within the laminate as shown in **Figure 2.3.** However, a damaged layer can still carry loads transverse to the fiber direction. Thus, from a macroscopic point of view, a broken layer can be considered a continuum with reduced Young's modulus transverse to the fibers, and shear modulus [9]. Nevertheless, after the first occurrence of IFF, if the load increases, further IFF cracks will rise rapidly in the respective layer as will be shown later in Chapter **4.1.3**.

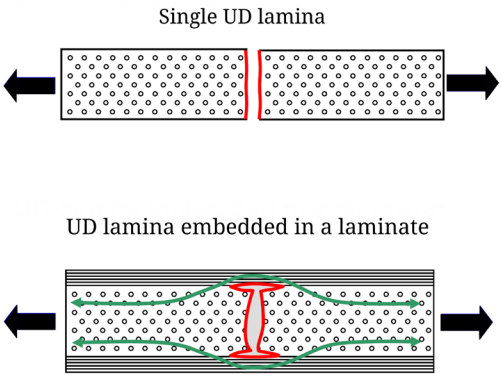

Figure 2.3. Local redistribution of forces, adapted from [9].

The importance of IFF for the loading capacity of a laminate ranges from safe to destructive, depending on the fracture plane orientation, the transmitted load, and the laminate lay-up [12]. If the direction of the load is the same as the fiber direction, the occurrence of an IFF is not critical; however, the integrity of a structure is vulnerable if the load direction is perpendicular to the fiber direction.

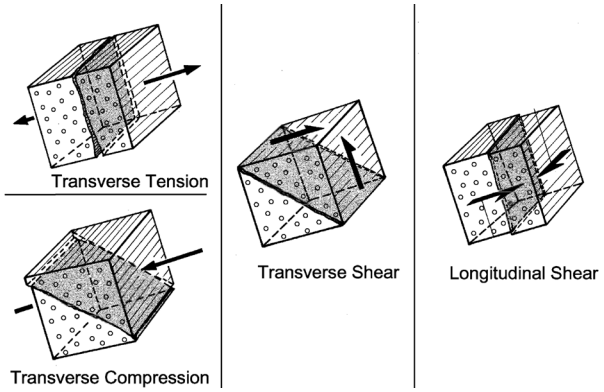

Figure 2.4. Types of IFF, from [9].

2.2.3. Delamination

Cracks formed in the interfacial plane between two plies in a laminate can cause separation of the plies and is referred to as delamination (see **Figure 2.5**). Tensile stresses acting in the thickness direction or shear stresses acting in planes parallel to the layer interfaces can result in local cracking in the interlaminar planes. Under cyclic loading, delamination zones grow and can make two adjacent lamina be separated from each other

[13]. Delamination can be a significant problem as it can annul the load transfer provided by shear stressing between layers reducing the laminate's stiffness and creating local instability.

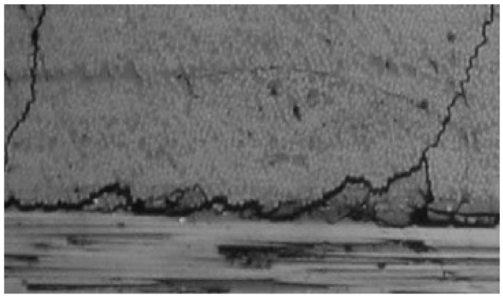

Figure 2.5. Delamination formed due to the joining of matrix damage, from [7].

2.2.4. Fiber Fracture (FF)

The fiber fracture (FF) marks the ultimate failure in a laminate [9]. The fiber fracture is not defined as the rupture of single filaments, but it is the rupture of most of the fiber of a lamina. In a unidirectional composite loaded in tension along fibers, the individual fibers fail at their weak points, and stress redistribution between fibers and matrix occurs. Under tensile stress (in the fiber direction), there is one fracture mode, and under compressive stress (in the fiber direction), three different fracture modes are possible, as shown in **Figure 2.6**.

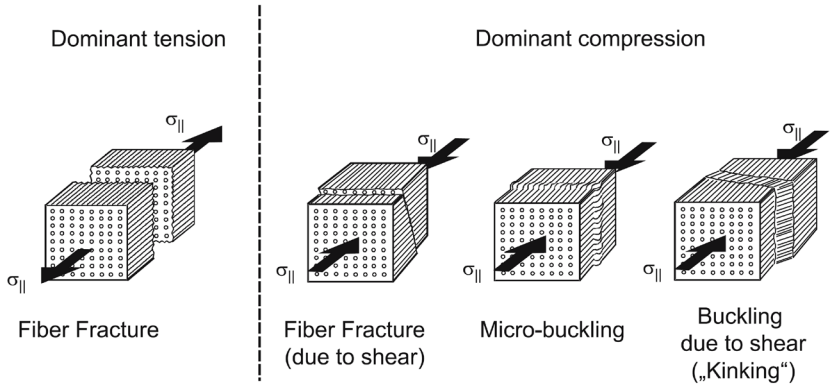

Figure 2.6. Types of FF, from [9].

2.3. FEA of laminates

The representation of composite materials in FE software can be focused on four scales: constituent level, lamina level, laminate level, and structural level (see **Figure 2.7**) [14].

At the constituent level, the observation scale is based on the fiber diameter. The fibers and the matrix are analyzed independently, and the interaction between them is considered. At the lamina level, the macro-mechanics analysis is considered. Fibers and the matrix are no longer differentiated, and the lamina is treated as a homogeneous anisotropic material. At the laminate level, the macro-mechanics analysis is also considered. The laminate is analyzed considering both lamina orthotropic properties and the stacking sequence. The interface between laminas is also considered. Lastly, the structure's whole components are considered at the structure level.

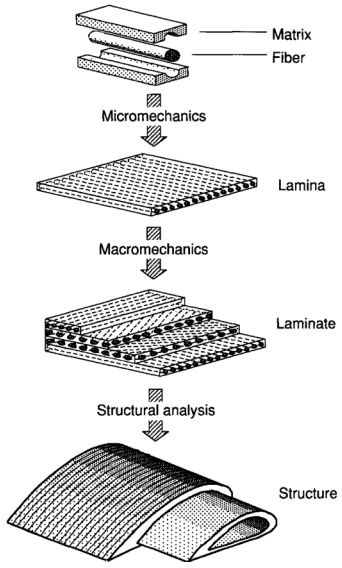

Figure 2.7. Scale of the analysis, from [14].

Over the years, many theories have been created to achieve the basic requirements for stress, strain, and displacement fields over the laminate's through-thickness direction [9]. Most approaches consider the lamina level scale of analysis. Three-dimensional analyses have shown that displacement and transverse stress must be continuous functions

(differentiable) in the laminate's through-thickness direction. Also, the transverse normal stress is crucial to describe the stress and strain through-thickness direction [15]. Therefore, based on these conclusions, two main groups of theories for modeling laminates can be classified into: Equivalent Single Layer (ESL) theories and Layer-Wise (LW) theories.

The models based on ESL theories consider the laminate as a homogeneous structure using through-thickness assumptions for the displacement [16], which reduces the 3D continuum analysis to a 2D one [17]. These theories are developed assuming that the displacement field is at least C^1 - continuous (function and its derivate are differentiable) through thickness [15]. In the commercially available FE software ABAQUS [18], this approximation is applied with shell or continuum shell elements (Ch. **2.3.1**). Using the models based on ESL theories requires only one element to represent all the laminate's thickness, and the accuracy of the simulation is controlled by changing the number of Gauss Points (GP) in the through-thickness direction. ESL theories work fine when describing thin composite laminates; however, they generally do not capture the complete three-dimensional stress field in considerably thick laminates [15], [19].

On the other hand, for the LW theories, each layer of the laminate is represented with its degree of freedom (DOF), having a separate displacement field for each layer, i.e., the number of unknown variables depends on the number of layers. Thus, the methods based on the LW theories are computationally more expensive than those used in the ESL theories, although achieving more accurate stress and strain fields in the laminate [15], [20]. To adopt the LW approach, solid continuum or continuum shell elements could be used in ABAQUS stacked on each other to form the whole laminate. Therefore, having at least one mesh element through thickness for each lamina of the laminate is crucial. Depending on the theory, one of the three-element types (Ch. **2.3.1**) must be chosen, as illustrated in **Figure 2.8** [9].

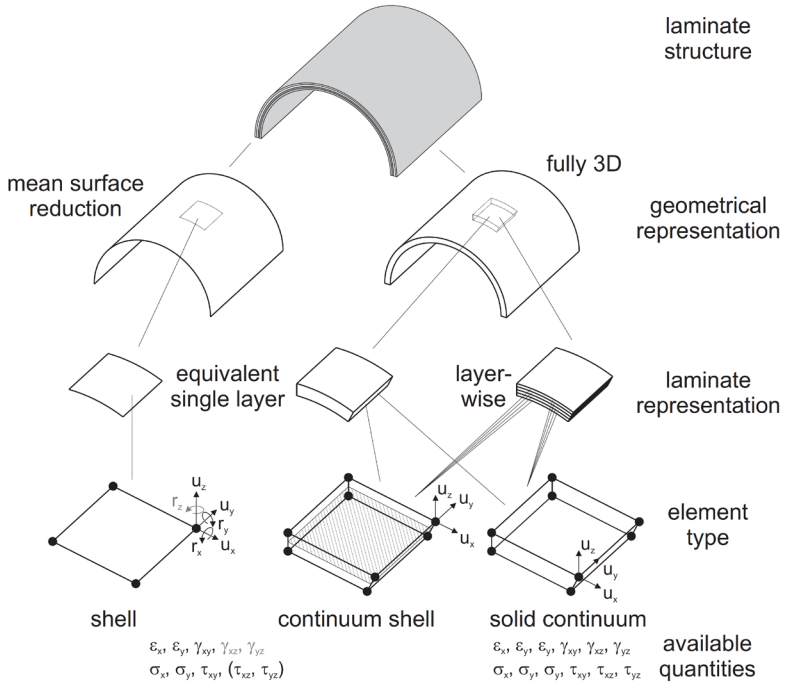

Figure 2.8. Element types for laminate structure FE representation, from [10].

2.3.1. Element types for laminates

In this section, it will be shortly described some aspects of shell, continuum shell, and solid continuum elements in ABAQUS software.

Solid continuum elements

The solid elements in ABAQUS are the standard volume elements with three translation degrees of freedom and usually consist of 4, 8, 10, or 20 nodes per element. They can be used for linear and complex nonlinear analyses involving contact, plasticity, and large deformations. These elements are not recommended for discretizing bodies with small thicknesses because their accuracy depends on balanced spatial proportions. Furthermore, linear 3D elements cannot capture bending because the edges do not deform, and, as a result fictitious shear stresses are introduced. This phenomenon is named shear locking and can be reduced using quadratic elements or using more elements through-thickness. However, both methods can be highly computationally expensive. Still, stress and strain components in the through-thickness direction make these elements very practical. Additionally, using the reduced-integration elements in ABAQUS, with only one gaussian point (integration point),

can cause distortion so that the strains calculated at the integration point are all zero, leading to uncontrolled distortion of the mesh. This scenario can be reduced by using the enhanced hourglass control option provided by ABAQUS.

Shell elements

Shell elements are 2D and consist of 2, 3, 4, 6, or 8 nodes. Besides the fact they are only 2D elements, they provide 6 DOF, including three rotation DOF at each node.

This is the most common element group used when the thickness of the geometry is small compared to the other dimensions. Shell elements provide the lower computational effort, and, in fact, that is the main reason why they are chosen. Depending on the model, this element type can considerably reduce simulation time without compromising the accuracy of the results. However, if accurate stress and strain profiles through-thickness are required, then shell elements are not applicable.

Continuum shell elements

These elements are the middle term between solid and shell elements. They look like three-dimensional continuum solids, but their kinematic and constitutive behavior is similar to conventional shell elements. They have four nodes per element, each with three displacement DOF. The thickness change is caused by Poisson's ratio, like shell elements, but also due to strain in the thickness. Continuum shell elements are computationally more expensive than conventional shell elements but less than 3D solid elements.

2.3.2. Laminate's coordinate system

It is essential to understand the different coordinate systems adopted in any analysis, including the one conducted in this work. Since each lamina has its coordinate system that varies with the orientation of the fibers, it is more convenient to analyze laminates using a common fixed system of coordinates (x, y, z), where z is always normal to the plane of the laminate.

2.3.3. Lamina's coordinate system

Considering the lamina scale of analysis, a single lamina in a laminate behaves as an orthotropic material. That is, it behaves differently along three mutually orthogonal planes. Their interception forms three axes: in the fiber direction x_1, the through-thickness direction x_3, and a third direction perpendicular to the other two x_2. This will be the adopted coordinate system when referring to the lamina's properties in the later described failure criterion.

2.4. Puck's failure criterion

A failure criterion's objective is determining if an arbitrary load leads to component fracture. Inspired by the Hashin's criterion [21], Alfred Puck developed a revolutionary fracture criterion, and a refined failure model characterized by considerable improvements compared to the criteria and models established.

In the first world-wide failure exercise (WWFE-I) [22], Puck's failure criterion comes out to be one of the five leading failure theories among all the nineteen participants [23]. In the second world-wide failure exercise (WWFE-II), Puck's fracture criteria and experimental results were in good agreement [12].

Puck's failure criterion can identify the different fracture modes in the FRP and effectively quantifies the effect of a detected fracture in one layer of a laminate on the laminate. In addition, Puck's criterion calculates the angle of the fracture plane θ_{fp}.

Puck's failure theory assumes transverse isotropy of the lamina and distinguishes two types of fracture: inter-fiber fracture (IFF) and fiber fracture (FF). This section will present the fracture types, their occurring conditions, and all the related mathematical formulations needed to implement Puck's failure criterion on the commercially available FEA software ABAQUS.

2.4.1. Stress analysis

Nine stress components define the state of the stress in one point of a continuum body. Of those, three are normal stresses $\sigma_1, \sigma_2, \sigma_3$ and the remaining ones are shear stresses $\tau_{12}, \tau_{13}, \tau_{21}, \tau_{23}, \tau_{31}$ and τ_{32} (see **Figure 2.9**). The first stress index indicates the plane the

stress is acting on. For instance, all the stresses starting with the index 3 act on a common action plane characterized by the direction of the normal vector "x_3". The second index specifies the direction of the stress. All the stresses with 2 in the second index act in the direction "x_2".

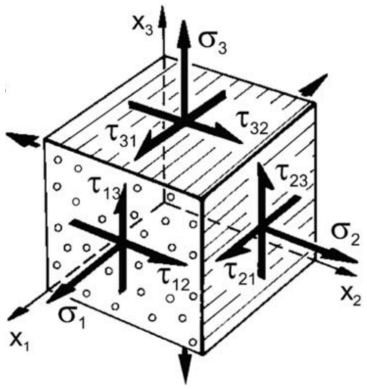

Figure 2.9. Definition of the three-dimensional direct stresses $\boldsymbol{\sigma_1, \sigma_2, \sigma_3}$ and shear stresses $\boldsymbol{\tau_{12}, \tau_{13}, \tau_{21}, \tau_{23}, \tau_{31}}$ and $\boldsymbol{\tau_{32}}$ in a UD lamina, from [12].

The term *stressing* is regularly used in Puck-related works (stressing means type of stress) [9]. This happens because of the transverse isotropy of the unidirectional (UD) lamina, i.e., stresses σ_2 and σ_3 affect the material in the same way. Thus, it is often helpful to talk not about stresses σ_2 and σ_3 but about the stressing $\sigma_\perp$. The same thing happens with shear stresses τ_{21} and τ_{31} that can be named longitudinal shear stressing $\tau_{\perp\parallel}$. Also τ_{23} can be named transverse shear stressing $\tau_{\perp\perp}$ and finally, normal stresses acting in the fiber direction $\sigma_\parallel$. All these *stressings* can be visualized in **Figure 2.10**.

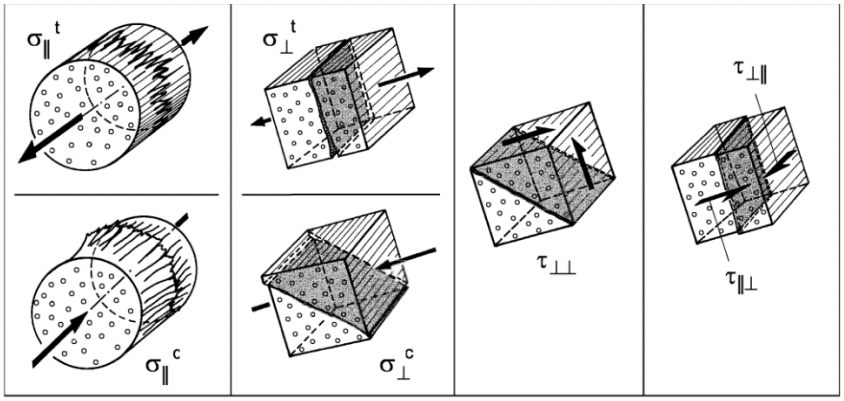

Figure 2.10. Types of *stressings* of a UD-composite element, from [9].

Lamina's constitute relations

The constitutive behavior is the law that relates stress states to strain states. The individual lamina is a homogeneous and anisotropic material, behaving equally in the transverse and through-thickness directions. Hence, this assumption, reduces the general anisotropy to a transversely isotropic behavior with only a fiber-parallel ∥ and fiber-perpendicular ⊥ directions. Consequently, the number of independent parameters required to evaluate the material stiffness matrix is reduced from to nine to five. For an orthotropic lamina, the stress-strain relations take the following form [24] :

$$\begin{Bmatrix} \sigma_1 \\ \sigma_2 \\ \sigma_3 \\ \tau_{12} \\ \tau_{23} \\ \tau_{31} \end{Bmatrix} = \begin{bmatrix} C_{11} & C_{12} & C_{13} & & & \\ & C_{22} & C_{23} & & & \\ & & C_{33} & & & \\ & & & 2G_{12} & & \\ & Sym. & & & 2G_{23} & \\ & & & & & 2G_{31} \end{bmatrix} \begin{Bmatrix} \varepsilon_1 \\ \varepsilon_2 \\ \varepsilon_3 \\ \varepsilon_{12} \\ \varepsilon_{23} \\ \varepsilon_{31} \end{Bmatrix} \tag{2.1}$$

If one of the failure modes occurs (Ch. 2.4), the constitutive relation parameters change based on the method "element weakening method (EWM)" [25]. In the presence of failure, the constitutive relation is modified by damage parameters d_f and d_m (Eq. **(2.3)** and **(2.4)**) associated with the fiber and matrix failure, respectively. The variables d_{ft}, d_{fc}, d_{mt} and d_{mc} are related to fiber and matrix damage under tensile and comprehensive stress states, respectively. These variables assume the value of 1 if their associated failure mode occurs. Hence, to account for the lamina failure possibility, the constitutive relation needs to include the failure modes with the EWM, as follows:

$$d_f = 1 - (1 - d_{ft})(1 - d_{fc}) \tag{2.2}$$

$$d_m = 1 - (1 - d_{mt})(1 - d_{mc}) \tag{2.3}$$

$$C_{11} = (1 - d_f)C_{11}^0 \tag{2.4}$$

$$C_{22} = (1 - d_f)(1 - d_m)C_{22}^0 \tag{2.5}$$

$$C_{33} = (1 - d_f)(1 - d_m)C_{33}^0 \tag{2.6}$$

$$C_{12} = (1 - d_f)(1 - d_m)C_{12}^0 \tag{2.7}$$

$$C_{23} = (1 - d_f)(1 - d_m)C_{23}^0 \tag{2.8}$$

$$C_{13} = (1 - d_f)(1 - d_m)C_{13}^0 \tag{2.9}$$

$$G_{12} = (1 - d_f)(1 - s_{mt}d_{mt})(1 - s_{mt}d_{mc})G_{12}^0 \tag{2.10}$$

$$G_{23} = (1 - d_f)(1 - s_{mt}d_{mt})(1 - s_{mt}d_{mc})G_{23}^0 \tag{2.11}$$

$$G_{31} = (1 - d_f)(1 - s_{mt}d_{mt})(1 - s_{mt}d_{mc})G_{31}^0 \tag{2.12}$$

$$C_{11}^0 = E_1(1 - \nu_{23}\nu_{32})\delta \tag{2.13}$$

$$C_{11}^0 = E_1(1 - \nu_{23}\nu_{32})\delta \tag{2.14}$$

$$C_{22}^0 = E_2(1 - \nu_{13}\nu_{31})\delta \tag{2.15}$$

$$C_{33}^0 = E_3(1 - \nu_{12}\nu_{21})\delta \tag{2.16}$$

$$C_{12}^0 = E_1(\nu_{21} + \nu_{31}\nu_{23})\delta \tag{2.17}$$

$$C_{23}^0 = E_2(\nu_{32} + \nu_{12}\nu_{31})\delta \tag{2.18}$$

$$C_{13}^0 = E_1(\nu_{31} + \nu_{21}\nu_{32})\delta \tag{2.19}$$

$$\delta = 1/(1 - \nu_{12}\nu_{21} - \nu_{23}\nu_{32} - \nu_{31}\nu_{13} - 2\nu_{21}\nu_{32}\nu_{31}) \tag{2.20}$$

where C_{ij}^0 and C_{ij} are the undamaged and damaged material stiffness components, respectively; E_1, E_2 and E_3 are Young's moduli in the three laminae directions (x_1, x_2, x_3) respectively; ν_{ij} are the Poisson's ratios that can be defined as $\nu_{ij} = -\varepsilon_j/\varepsilon_i$, with $i \neq j$, and G_{12}, G_{23} and G_{31} are shear moduli in $x_1 - x_2$, $x_2 - x_3$ and $x_3 - x_1$ planes, respectively. Lastly, s_{mt} and d_{mt} are the loss control factors for the shear stiffness caused by the matrix tensile and compressive failures, respectively. In this study, the used loss control factors values were: $s_{mt} = 0.9$ and $s_{mt} = 0.5$ as used in work by Seung Lee et.al. [25].

2.4.2. Inter-Fiber Fracture criterion (IFF)

The Puck's Inter Fiber Fracture criteria was developed based on important experimental evidence. In 1997, a large research project was developed in Germany, where carbon and glass FRP were tested [9]. **Figure 2.11** shows the results of glass and carbon FRP multiaxial stress states strength tests.

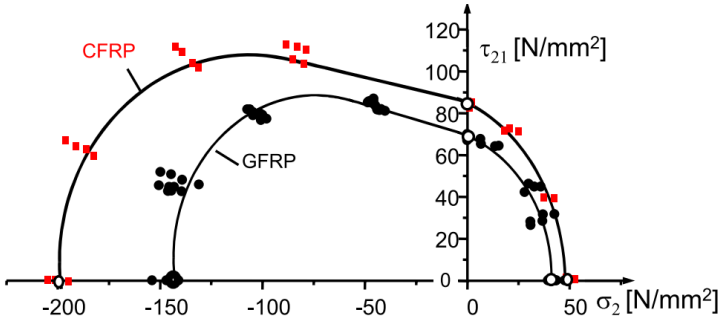

Figure 2.11. Fracture limits for (σ_2, τ_{21})-stress combinations, from [9].

From that study, three important conclusions were drawn:

- The stresses σ_2^t and τ_{21} interact. If the two stresses act once, the fracture occurs before $\sigma_2^t = R_\perp^t$ or $\tau_{21} = R_{\perp\parallel}$ where $R_\perp^t$ and $R_{\perp\parallel}$, are the resistances of the action plane, which will be explained later in Chapter 2.4.2.1;
- Under moderate transverse compressive stress σ_2^c, a higher shear stress τ_{21} can be sustained;
- When σ_2^c and τ_{21} act simultaneously and their ratio exceeds a certain value, the fracture appears in a plane with an angle $\theta_{fp} \neq 0$, as illustrated in Figure 2.13.

Accordingly, there are three types of IFF: *Mode A, Mode B,* and *Mode C.* The Master Fracture Body (MFB), represented in **Figure 2.12** helps understand those different modes. In this figure, the outer surface consists of all points representing combinations of stresses σ_n , τ_{nt}, τ_1 which produce an inter-fiber fracture (IFF).

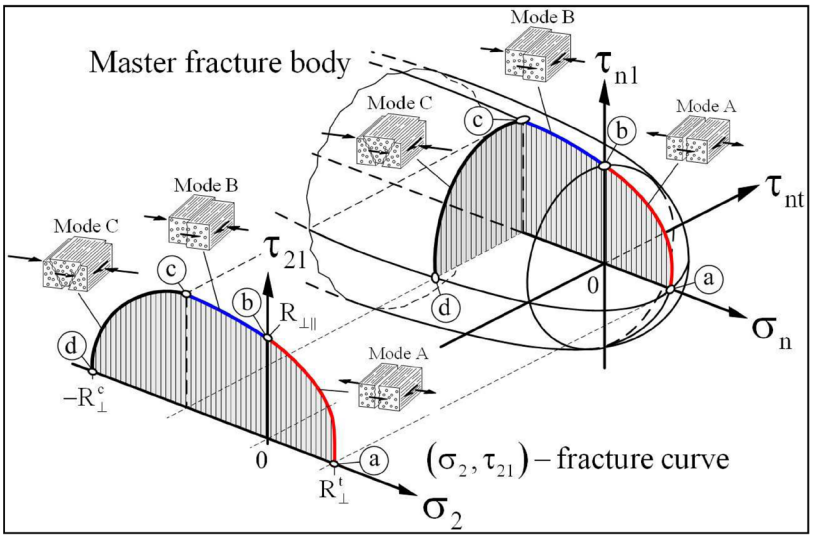

Figure 2.12. Master fracture body, from [26].

In the *Mode A*, the fracture surfaces are separated due to tensile stressing leading to a degradation of Young's modulus transverse to fiber $E_{\perp}$ and the shear modulus $G_{\perp\parallel}$. The stressings responsible for this failure mode are the transverse tensile stressing $\sigma_{\perp}^{t}$ and the longitudinal shear stressing $\tau_{\perp\parallel}$, acting alone or in combination.

In the *Mode B,* the fracture is caused by longitudinal shear stressing $\tau_{\perp\parallel}$. In this case, the normal transverse shear stressing acting on the action plane is compressive $\sigma_{\perp}^{t}$. Hence, the crack does not open, and the fracture surfaces are pushed on each other. This failure mode does not significantly change the stiffness of the lamina.

Dissimilarly to the other modes of IFF, in the *Mode C,* the fracture's plane is inclined, and the angle of the fracture plane θ_{fp} can vary from 0 to 54º, as illustrated in **Figure 2.13**. This mode occurs only when the ratio of compressive normal stressing and the transverse compressive strength, $\sigma_{\perp}^{c}/R_{\perp}^{c}$ is higher than approximately 0.4 [9].

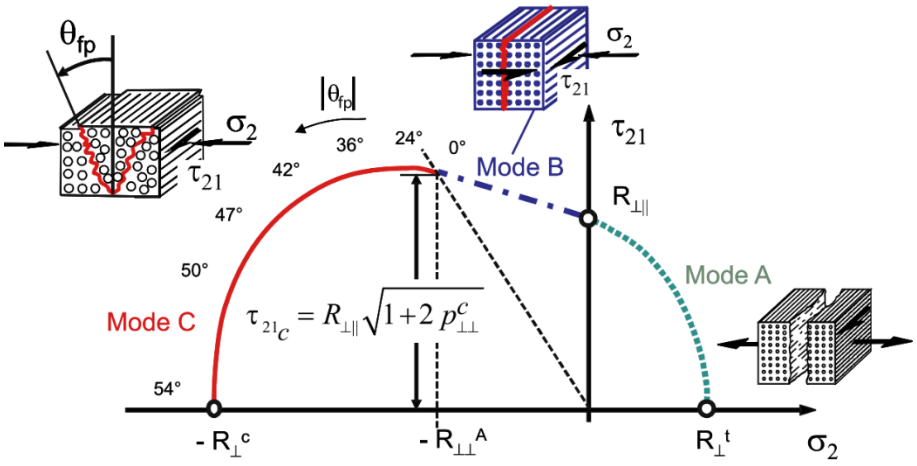

Figure 2.13. Fracture curve ($\boldsymbol{\sigma_2}, \boldsymbol{\tau_{21}}$), from [9].

2.4.2.1. Stress and resistance of the action plane

A central conclusion from Puck's considerations is that three stresses act on a common action plane (σ_n, τ_{nt} and τ_{n1}). Puck suggested a rotated coordinate system around the x_1 axis by an angle θ. The angle θ is measured counterclockwise starting from the x_3 axis as shown in **Figure 2.14**. Three new stresses $\sigma_n(\theta), \tau_{nt}(\theta), \tau_{n1}(\theta)$ can be obtained from stresses $\sigma_2, \sigma_3, \tau_{21}, \tau_{23}, \tau_{31}$ using the Equations **(2.21)**, **(2.22)** and **(2.23)** [27]:

$$\sigma_n(\theta) = \sigma_2 \cos^2\theta + \sigma_3 \sin^2\theta + 2\tau_{23} \sin\theta \cos\theta \tag{2.21}$$

$$\tau_{nt}(\theta) = -\sigma_2 \sin\theta \cos\theta + \sigma_3 \sin\theta \cos\theta + \tau_{23}(\cos^2\theta - \sin^2\theta) \tag{2.22}$$

$$\tau_{n1}(\theta) = \tau_{31} \sin\theta + \tau_{21} \cos\theta \tag{2.23}$$

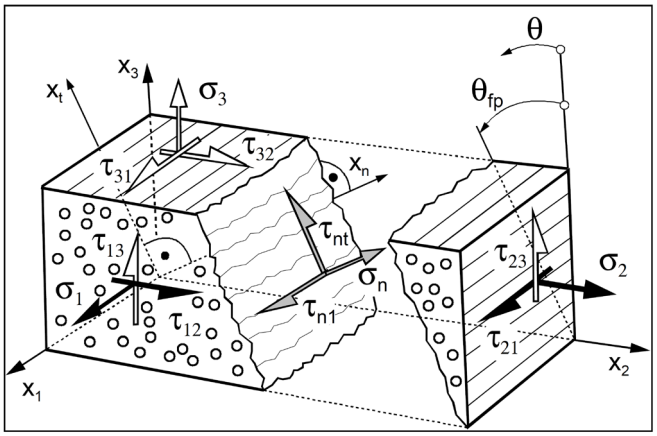

Figure 2.14. Action plane stresses and fracture angle, from [26].

These three new stresses acting on the common action plane need to be related to the strengths of the action plane. In simplified terms, these strengths are the amount of resistance that the action plane can handle in response to one of the stressings $\sigma_{\perp}$, $\tau_{\perp\parallel}$ or $\tau_{\perp\perp}$. To accurately distinguish these strengths and the common strengths of a UD-lamina, Puck announced the *fracture resistance of the action plane* R^A.

For better understanding and to avoid confusing on the resistance of the action plane R^A and the strength of a UD-lamina, the reader should be aware of the following terminology used for the strengths[1] of the UD-lamina:

$R_{\parallel}^{t}$: Fiber parallel tensile strength;

$R_{\parallel}^{c}$: Fiber parallel compressive strength;

$R_{\perp}^{t}$: Transverse tensile strength;

$R_{\perp}^{c}$: Transverse compressive strength;

$R_{\perp\perp}$: Transverse shear strength;

$R_{\perp\parallel}$: Longitudinal shear strength;

and for the resistance of the fracture plane:

$R_{\perp}^{A\,t}$: Resistance of the action plane to transverse tensile stressing $\sigma_{\perp}^{t}$;

$R_{\perp\perp}^{A}$: Resistance of the action plane to transverse shear stressing $\tau_{\perp\perp}$;

$R_{\perp\parallel}^{A}$: Resistance of the action plane to longitudinal shear stressing $\tau_{\perp\parallel}$;

[1] Always positive values.

If the fracture and the action plane coincide in a specific stress state, the strength of the material and the fracture resistance of the action plane have the same value. For a better understanding, if a tensile stressing $\sigma_{\perp}^{t}$ is applied to a UD-lamina and lead to a fracture, then the fracture plane will coincide with the action plane, and the transverse tensile strength of the UD lamina, $R_{\perp}^{t}$, will correspond to the resistance of the action plane $R_{\perp}^{A\,t}$. Similarly, when applied a longitudinal shear stressing, $\tau_{\perp\parallel}$, the fracture plane and the action plane are the same, so $R_{\perp\parallel}^{A} = R_{\perp\parallel}$.

Distinctly, the $R_{\perp\perp}^{A}$ is very different from the transverse shear strength, $R_{\perp\perp}$, and a detailed explanation for that can be found in the work of Lutz [27]. To obtain $R_{\perp\perp}^{A}$, an inclination parameter $p_{\perp\perp}^{c}$ is required, as shown in Equation **(2.24)** [25].

$$R_{\perp\perp}^{A} = \frac{R_{\perp\parallel}}{2p_{\perp\parallel}^{c}}\left(\sqrt{1 + 2p_{\perp\parallel}^{c}\frac{R_{\perp}^{c}}{R_{\perp\parallel}}} - 1\right) \tag{2.24}$$

The experimentally determined inclination parameters $p_{\perp\parallel}^{t}$, $p_{\perp\parallel}^{c}$ $p_{\perp\perp}^{t}$ and $p_{\perp\perp}^{c}$ can be deducted from the fracture curve illustrated in Figure 2.13 [26]. All the recommended inclination parameters for GFRP are summarized in **Table 2.1**:

Table 2.1. Recommended inclination parameters for GFRP, from [9].

$p_{\perp\parallel}^{t}$	$p_{\perp\parallel}^{c}$	$p_{\perp\perp}^{t}, p_{\perp\perp}^{c}$
0.30	0.25	0.20 - 0.25

2.4.2.2. Fracture plane

To determine if a plane can sustain a specific load, first, the plane's fracture angle θ_{fp} needs to be detected. The fracture plane is defined as the action plane with the maximum local stress exposure, as Equation **(2.25)** shows, and the local stress exposure, f_E, can be used as a direct measure of the fracture risk since it grows linearly with the stresses [9]. Therefore, the f_E is calculated for all sections between $\theta = [-90^{\circ}; 90^{\circ}]$ to find the fracture plane,

meaning that if the search step is 1º, there are 180 calculations for each element to evaluate the fracture plane. However, this numerical effort is no longer a problem with today's computer technology [9]. Note that the fracture plane is under the higher local stress exposure stress, but it will not fail if the stressing is lower than the resistance of the action plane R^A.

$$[f_E(\theta_{fp})] = [f_E(\theta)]_{max} \tag{2.25}$$

The local stress exposure f_E can be calculated with the expressions that constitute Puck's IFF criterion, using the Equations **(2.26)** and **(2.27)** [28]:

For $\sigma_n \geq 0$

$$f_{E,IFF}(\theta) = \sqrt{\left[\left(\frac{1}{R_{\perp}^{At}} - \underbrace{\frac{p_{\perp\psi}^{t}}{R_{\perp\psi}^{A}}}_{\text{Eq. (2.28)}}\right)\underbrace{\sigma_n(\theta)}_{\text{Eq. (2.21)}}\right]^2 + \left(\underbrace{\frac{\tau_{nt}(\theta)}{R_{\perp\perp}^{A}}}_{\text{Eq. (2.24)}}\right)^2 + \left(\overbrace{\frac{\tau_{n1}(\theta)}{R_{\perp\parallel}^{A}}}^{\text{Eq. (2.23)}}\right)^2} + \frac{p_{\perp\psi}^{t}}{R_{\perp\psi}^{A}}\sigma_n(\theta) \tag{2.26}$$

For $\sigma_n \leq 0$

$$f_{E,IFF}(\theta) = \sqrt{\left(\underbrace{\frac{p_{\perp\psi}^{c}}{R_{\perp\psi}^{At}}}_{\text{Eq. (2.29)}}\sigma_n(\theta)\right)^2 + \left(\frac{\tau_{nt}(\theta)}{R_{\perp\perp}^{A}}\right)^2 + \left(\frac{\tau_{nl}(\theta)}{R_{\perp\perp}^{A}}\right)^2} + \frac{p_{\perp\psi}^{c}}{R_{\perp\psi}^{A}}\sigma_n(\theta) \tag{2.27}$$

where:

$$\frac{p_{\perp\psi}^{t}}{R_{\perp\psi}^{A}} = \frac{p_{\perp\perp}^{t}}{R_{\perp\perp}^{A}}\cos^2\psi + \frac{p_{\perp\parallel}^{t}}{R_{\perp\perp}^{A}}\sin^2\psi \tag{2.28}$$

$$\frac{p_{\perp\psi}^{c}}{R_{\perp\psi}^{A}} = \frac{p_{\perp\perp}^{c}}{R_{\perp\perp}^{A}}\cos^2\psi + \frac{p_{\perp\parallel}^{c}}{R_{\perp\perp}^{A}}\sin^2\psi \tag{2.29}$$

$$cos^2\psi = \frac{\tau_{nt}^2}{\tau_{nt}^2 + \tau_{nl}^2} \quad (2.30)$$

$$sin^2\psi = \frac{\tau_{nl}^2}{\tau_{nt}^2 + \tau_{nl}^2} \quad (2.31)$$

After calculating the angle of the fracture plane θ_{fp}, the same expressions are used to verify if the failure occurs using the detected θ_{fp} [9]. Failure occurs if $f_{E,IFF}\left(\theta_{fp}\right) \geq 1$. The chosen path to predict IFF failure does not provide direct information about the IFF failure modes. However, that information is not relevant to the scope of this dissertation.

2.4.3. Fiber fracture criterion (FF)

Fiber fracture is mainly caused by stressing parallel to the fibers $\sigma_{\parallel}$. Since the lamina is treated as a homogenized orthotropic continuum, the exact stresses parallel to the fiber direction acting in the fiber cannot be identified. Hence, the stress exposure $f_{E,FF}$, is a ratio of the homogenized stress σ_1 in the lamina parallel to the fiber direction to the resistance of the lamina in fiber direction. Furthermore, the transverse stresses σ_2 and σ_3 influence the strain in fiber direction due to the Poisson's effect, and because of the lamina's non-homogeneity, the Poisson's effect is magnified locally, close to fibers. Therefore, Puck accounts for this phenomenon by using a magnification factor m_{σ_f}. The resulting fiber fracture criterion formulation can be directly understood as a formulation for stress exposure as shown in Equation **(2.32)** [28]:

$$f_{E,FF} = \frac{1}{\pm R_{\parallel}^{t,c}} \underbrace{\left[\sigma_1 - \left(\nu_{\perp\parallel} - \nu_{\perp\parallel f} m_{\sigma_f} \frac{E_{\parallel}}{E_{\parallel f}}\right)(\sigma_2 + \sigma_3)\right]}_{A} \quad (2.32)$$

$$with \begin{cases} R_{\parallel}^{t} \; for \; A \geq 0 \\ -R_{\parallel}^{c} \; for \; A < 0 \end{cases}$$

where $\nu_{\perp\|}$ is the major Poisson's ratio of the fiber, $E_{\|}$ is the lamina longitudinal modulus that is parallel to the fibers, while $E_{\|f}$ is the fiber longitudinal modulus. Also, m_{σ_f} is the magnification factor for the transverse stress in the direction of the fiber. For this work, the $m_{\sigma_f}$was set to 1.3, as recommended for GFRP by Lee et al. [9].

2.5. Effects of seawater exposure on composites

During its service, a fiber-reinforced polymer (FRP) will absorb moisture from its surroundings which leads to a general reduction of its mechanical properties [29], [30].

Andreoppoulos et al. [30] suggest two possible mechanisms responsible for reducing mechanical properties: matrix plasticization and/or degradation of the fiber-matrix interface. The degradation of the fiber-matrix interface bounding is the most prejudicial [31].

2.5.1. Water absorption

Water absorption of the composites is a complex behavior, which many causes can influence, such as the resin and cured agent, void content, fabrication, fiber volume fraction, orientation of reinforcement, area of exposed surfaces, temperature, among others [32], [33]. The moisture penetration is mainly conducted by diffusion [34], and most water absorption is commanded by diffusion and absorbed in the matrix. Water also enters into the FRPs by the fiber/matrix interface capillarity and microcracks. These last two methods are often damage-dependent since a damaged composite is able to absorb considerably more water [33]. The capillarity mechanism involves the flow of water molecules along the fiber–matrix interface, followed by diffusion from the interface into the bulk resin. The transport of moisture by microcracks involves both the flow and storage of water in microcracks or other forms of microdamage [35].

Over the years, numerous diffusion models have been proposed to model the diffusion process. The one-dimensional Fickian model is probably one of the most used due to its simplicity, and can be written in the form [36]:

$$\frac{\partial c}{\partial t} = D_{Coef} \frac{\partial^2 C}{\partial x^2} \tag{2.33}$$

where x is the coordinate parallel to the diffusion direction, D_{Coef} is the diffusion coefficient in the x-direction, and C is the moisture concentration. The moisture absorption contend M_t is time-dependent and can be approximated by the following equation [36]:

$$M_t(t) = M_\infty \left\{1 - \exp\left[-7.3\left(\frac{D_{Coef} t \times 3600 \times 24}{h^{\,2}}\right)^{0.75}\right]\right\} \tag{2.34}$$

where M_∞ is the maximum amount of absorption, t is time in days. The following equation allows obtaining the diffusion coefficient D_{Coef}, using two points at time t_1 and t_2 from the linear part of Fickian diffusion curve as:

$$D = \pi\left(\frac{hk}{4M_\infty}\right)^2 \tag{2.35}$$

where, h is the thickness, and k can be obtained as suggested by Wand et al. [36]:

$$k = \left(\frac{M_1 - M_2}{\sqrt{t_1} - \sqrt{t_2}}\right) \tag{2.36}$$

A crucial aspect to mention is the change in water absorption rate with the temperature. Pritchard and Speake [37] studied the kinetics of moisture absorption on GFRP for temperatures between 30 and 100 ºC, and, as **Figure 2.15** shows, the saturation point is reached more quickly with higher temperatures. However, the maximum water absorption remains equal.

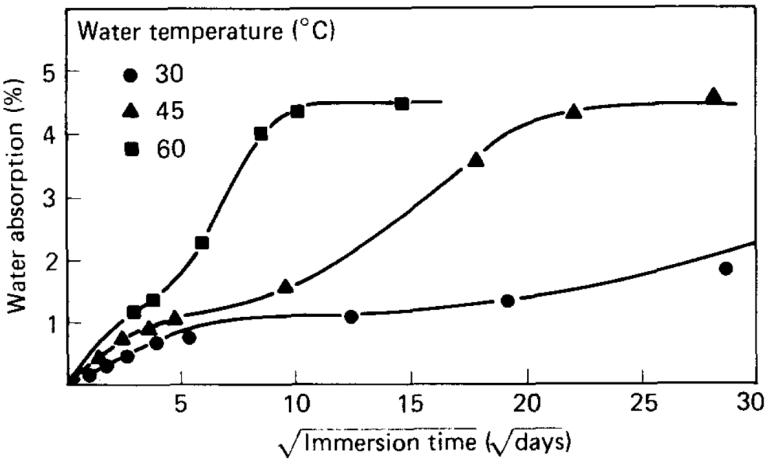

Figure 2.15. Water absorption kinetics with temperature, from [37]

2.5.2. Effects on mechanical properties

The previous study showed that the residual mechanical properties were found to be functions of true absorbed water content [37]. It was also recognized that after saturation, no change in the mechanical properties occurred and that water temperature does not change the tensile strength but the water absorption rate.

Saadatmanesh et al. [38] studied the effects of different aggressive environments on the tensile properties of different FRP, and the carbon FRP, when exposed to most environments, revealed excellent durability. Even after 27 months of exposure, the mechanical properties of the specimens were minimally affected by these environments. However, the exposure effects were significantly higher in the glass FRP specimens. Unidirectional laminates were tested with two types of glass fiber ($650 g/m^2$ and $400 g/m^2$) and one type of carbon fiber. The results of tensile strength tests are presented in **Figure 2.16**. After 20 000 hours of exposure, the normalized ultimate strength of the carbon specimens decreased by around 10%, while the glass-fiber ones decreased by 30 to 40%. Similarly, the ultimate strain dropped by 50% after the 20,000 hours of exposure time on the glass specimens. However, on the carbon specimens, the strain to failure values increased. Regarding Young's modulus, it increased on the GFRP specimens by approximately 10%. It is important to notice that the three specimens revealed a similar behavior, i.e. the strength remained approximately constant after a certain period. This behavior was also verified in the studies mentioned above [37].

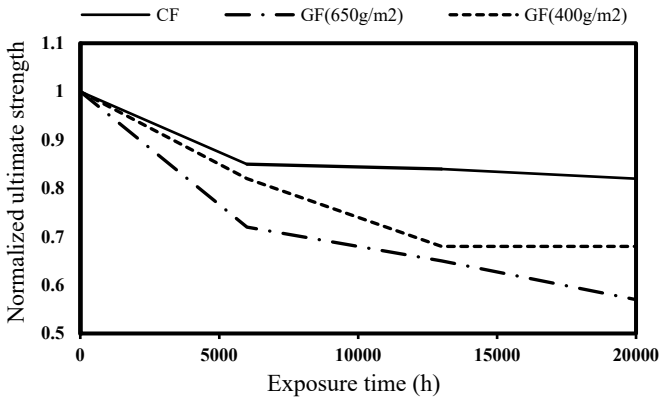

Figure 2.16. Normalized values of ultimate tensile strengths versus exposure time for laminates, adapted from [38].

Bian et al. [33] showed that the tensile strength of glass FRPs was reduced by 13% after only 42 days of immersion. Additionally, Gellert and Turley [39] conclude that the flexural strength continued to degrade for the GFRPs as water uptake continued toward saturation. Moreover, they reported strength losses between 15 and 21%. In addition, the interlaminar shear strength decreased by 21% after 485 days of immersion.

2.6. FEA method

ABAQUS uses implicit time integration methods to calculate the response of a system in the case of a quasi-static analysis. On the other hand, the dynamic analysis uses explicit integration [18]. Generally, the selection between the dynamic or quasi-static formulation is associated with efficiency, simulation precision, and the importance of inertia in the analysis [40].

In the quasi-static formulation, the inertia terms are neglected in the equilibrium equations of the body when compared to the forces involved in the processes. In ABAQUS, the quasi-static formulation uses the Backward Euler time integration. Because it is an implicit method, numerous simultaneous nonlinear dynamic equilibrium equations must be solved at each time increment. Based on Newton's method, this iterative process ends when the convergence criterion is reached. In this stage, convergence problems can occur forcing to reduce the time increment. For each iteration in a nonlinear analysis, ABAQUS forms the model's stiffness matrix and solves a system of equations. In practice, the computational cost

of one iteration is equivalent to that of conducting a complete linear analysis. Furthermore, the quasi-static formulation is mesh-dependent because of the nonlinear equilibrium equations. The simulation time can nearly quadruplicate with an increase in the number of elements [41], as will be verified in Chapter 4.

In the other hand, in an explicit dynamic analysis, the inertia terms are considered. Displacements and velocities are calculated based on values known at the beginning of the increment; hence, since the process does not require equilibrium iterations, the increment is less expensive than the increments in implicit integration.

In terms of increment stability, the size of the time increments of the explicit formulation is related to the stress wave size crossing the smallest element. Thus, the time increment in an explicit dynamic analysis can be very short, if the mesh has a small element or if the stress wave speed in the material is high. The Equation **(2.37)** allows to calculate an approximation of the time increment stability limit:

$$\Delta t \approx \frac{L_{min}}{c_d} \tag{2.37}$$

where L_{min} is the smallest element dimension in the mesh, and c_d is the dilatational wave speed. For the simulation of fast processes with fine meshes, a huge number of increments may be necessary. However, this process can be used, when inertia does not play a significant role, accelerated by artificially increasing the masses of the bodies.

The implicit analysis, however, is unconditionally stable; thus, there is no limit on the time increment size; the accuracy dictates the increment size.

The implementation of Puck's theory into the user-defined material depends on the FEA method. Therefore, since Puck's theory has been developed and verified for nonrecurring, uninterrupted, slow loading processes [10], the quasi-static domain is the proper FEA method.

3. MATERIALS AND METHODS

The main objective of this work is to formulate a numerical model capable of predicting the seawater effects on stress-strain behavior of GFRPs. The previous chapter featured all the theoretical foundations needed for the development of the model.

This chapter primarily presents details about the specimen's geometry used in previous works and some results from those works that later will be used to validate the numerical model. It then explains the laminate's modeling procedure, including a detailed explanation of the user sub-routine used to implement the Puck's failure criterion and the seawater exposure damage model. Lastly, the methodology used to develop the numerical model is adressed.

3.1. Experimental results

Gonçalves in 2019 [42] and Jorge [43], and Aguiar [44] in 2021 studied the effects of seawater on monotonic and fatigue responses of glass fiber reinforced polymers. The tested specimens had the geometry exhibited in **Figure 3.1**.

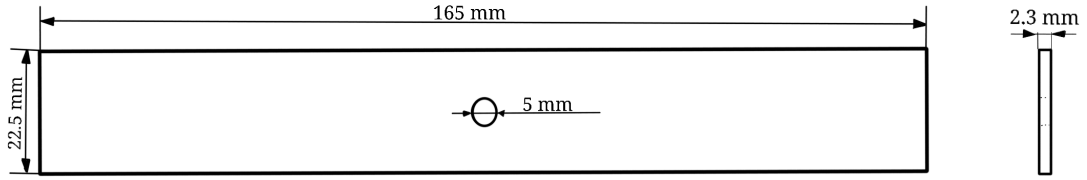

Figure 3.1. Geometry and dimensions of the specimen, from [42].

Tables 3.1 and 3.2 summarize some results of tensile strength tests for specimens not immersed and immersed for 900 days on seawater, respectively, conducted in the works mentioned above. It is important to mention that the composite specimens were hand-made and did not have exactly the same geometry in all the performed tests [43], which may justify some scatter.

Table 3.1. Maximum load and displacement at failure for control specimens (not immersed), from [37].

Nº	Maximum load, F [N]	Maximum displacement, δ [mm]
1	8969	2.87
2	9545	3.19
3	9155	2.33
Average	9223	2.797
St. Dev.	207.86	0.3549

Table 3.2. Maximum load and displacement at failure for specimens immersed for 900 days.

Nº	Maximum load, F [N]	Maximum displacement, δ [mm]
1	8380	2.69
2	7566	1.352
3	7475	2.16
Average	7807	2.068
St. Dev.	406.7	0.55

During the tensile tests, the specimens were fixed to the testing machine using grips instrumented with a load cell. The gripping force was controlled by adjusting the grip pressure on the specimen, and, the load increased until the total failure with a displacement rate of 2 mm/min.

The samples were immersed for 229 and 900 days, and then the mass was measured (before and after immersion) to determine the amount of water absorption (see **Table 3.3**).

Table 3.3. Water absorption after 229 and 900 days, from [42], [43]

Immersion time (days)	Water absorption (% m_d)
229	0.655
900	1.04

The load vs. displacement curves obtained in the experimental tensile tests for specimens immersed for 0 and 900 days are illustrated in **Figure 3.2**. The results revealed that the seawater reduced the ultimate tensile strength and increased the overall stiffness.

The control specimen manifested two different stages in terms of stiffness; initially, when loaded under 1.5 kN, it revealed a more brittle behavior, similar to the one exposed to seawater, and in the second phase, when loaded over 1.5 kN, it presented a more ductile behavior failing at approximately 9.0 kN. This behavior is probably due to the crack density increase as the load is being applied. In opposition, the control specimen revealed the same behavior in all the load ranges failing at approximately 7.3 kN.

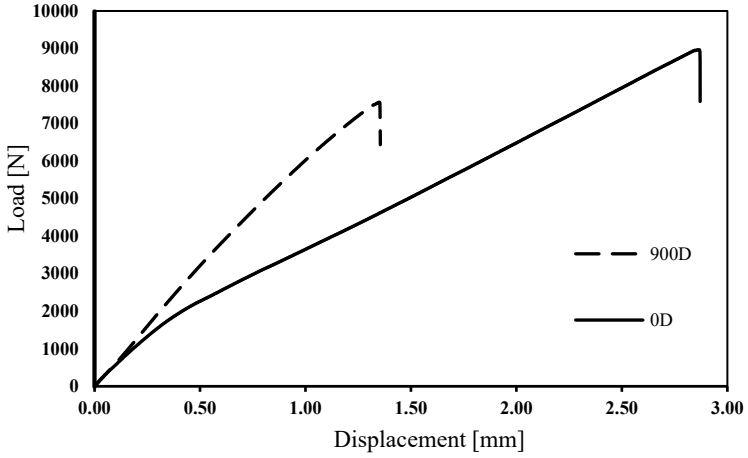

Figure 3.2. Longitudinal tensile test: load vs. displacement curves for specimens immersed for 0 and 900 days, from [44].

3.2. FEA procedure

The previously mentioned glass FRP was modeled in the commercially available FEA software ABAQUS with the composite layout [0º,45º,90º,45º,0º,90º]s as shown in Figure 3.3.

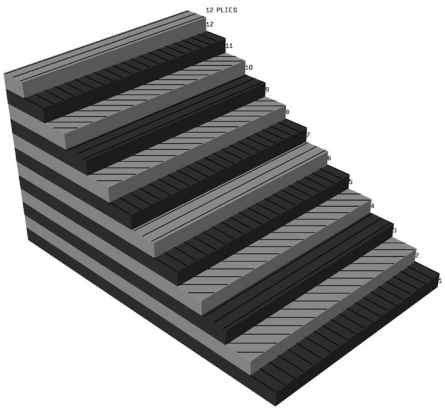

Figure 3.3. Laminate's ply layout in ABAQUS.

The layer-wise theory (Ch. **2.3**) was adopted using C3D8R elements, and the material properties are the same as recommended by the WWFE [22]. These reduced integration linear hexahedral elements only have one integration point in the element's centroid, which provides excellent benefits as the number of evaluations during the simulation is reduced substantially. However, this difference between the nodes and the integration points can lead to mesh instability known as hourglassing [45]. Hence, the enhanced hourglass control option was on for all the simulations.

Regarding mesh quality and mesh density, they are directly linked with solution accuracy. Finer meshes lead to more accurate results but also require more computational effort. Hence, the mesh must be only fine enough to obtain good results; otherwise, simulation speed can be lower without accomplishing improved solutions. Refining the critical zones is a recurrent way to reduce simulation time without sacrificing the solution's precision. Since the specimen's center zone is the one experiencing higher stresses, the chosen element size for that region was 0.1 mm. As the element's distance to the center zone increases, the elements are coarser, eventually measuring 3.5mm. One element through-thickness for each lamina was used (Ch. **2.3**). The chosen mesh consists of 123 262 elements and 146 874 nodes and is represented in **Figure 3.4**.

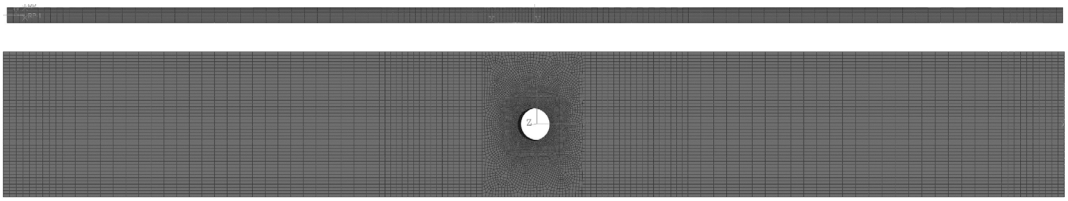

Figure 3.4. Representation of the mesh.

To simulate the tensile tests, it was necessary to define the boundary conditions. Hence, kinematic constraints were used in zones A and B, represented in **Figure 3.5**, and defined in **Table 3.4**.

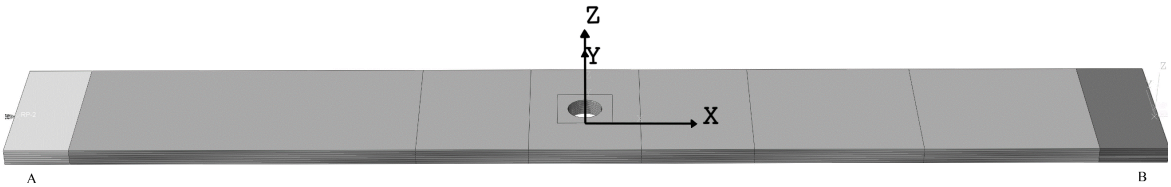

Figure 3.5. Representation of the regions where the boundary conditions were applied.

Table 3.4. Boundary conditions.

	U_x	U_y	U_z	R_x	R_y	R_z
A	×	×	×	×	×	×
B	✓	×	×	×	×	×

Regarding the FEA method, although the quasi-static analysis is particularly stable for large time steps, using lower time steps leads to improved solutions, resulting in higher simulation time. Hence, in all simulations, a time step of 0.01s was used, while the total time of 1 second was simulated.

3.2.1. UMAT sub-routine

ABAQUS allows users to modify the existing material models with the user sub-routines. The UMAT ("User material") sub-routine written in Fortran 95 was used in this work. The UMAT is associated with the analysis and requested by ABAQUS at every Gauss point for each increment (12,326,200 times/simulation with the current mesh and time step). This process can be visualized in **Figure 3.6**.

In each time increment and during the iterative procedure, the information on the material properties, strain tensor, strain incrementation, and the state variables are passed to the UMAT subroutine. After sending that information, if the iteration is the first one, the *Waterdamage* routine is called. This condition reduces simulation time since this routine requires data that do not vary with the increment number. The flowchart of that subroutine can be consulted in Appendix B. Concisely, the routine verifies if the integration point is within the zone damaged by the seawater and, if so, the tensile and compressive strengths parallel and perpendicular to fiber are degraded $R_{\parallel,\perp}^{t,c}$. Then, the constitutive matrix is computed, and, following that, the stress tensor is calculated. In the next step, the *SearchFP* routine is called which calculates the θ_{fp}. Its flowchart can also be consulted in Appendix B. After that, both IFF(Ch. **2.4.2**) and FF(Ch. **2.4.3**) failure criteria are verified. The respective degradation law is applied if a failure occurs. Then, since the constitutive matrix can change in the case of failure, the failure criteria must be verified again. Finally, the state variables are updated, and the updated constitutive matrix, the stress tensor and the state variables are sent to ABAQUS. Convergence is achieved if the residual force is lower than the tolerance value. If it is higher, the increment is repeated with a lower increment time to ensure easier convergence.

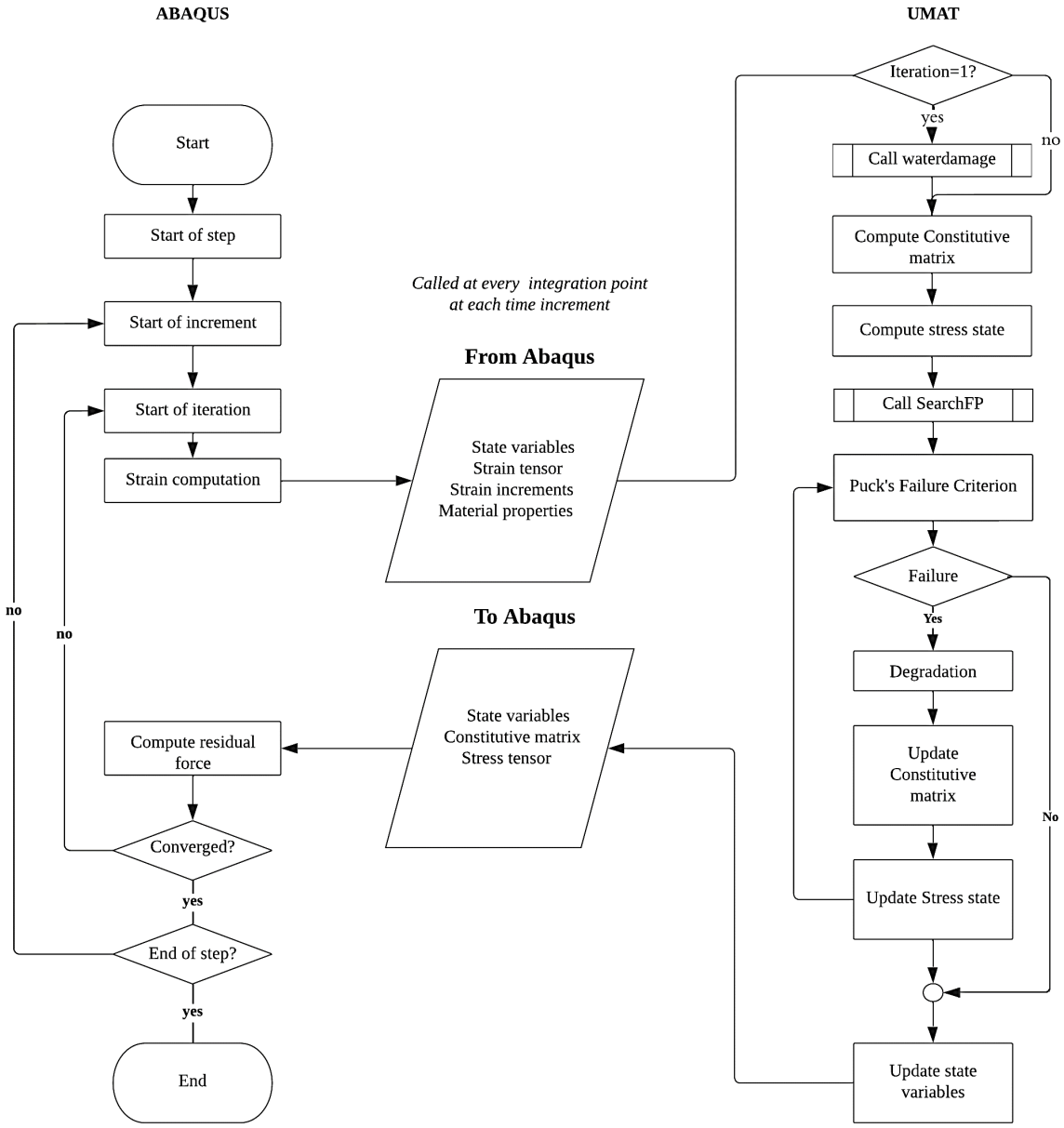

Figure 3.6. Structure of the user material subroutine (UMAT).

3.2.2. Seawater exposure damage model

As mentioned in Section **2.5.2**, the ultimate strength of GFRP is a function of the water absorption, and no perceptible damage development occurs after saturation. Accordingly, the damage done by the seawater must be a function of the amount of seawater in a specific specimen location. Considering this fact, the proposed numerical model degrades the material properties as a function of seawater concentration. The properties to be degraded are the tensile strength parallel and perpendicular to fiber and the compressive strength parallel and perpendicular to fiber $R_{\perp,\parallel}^{t,c}$. Also, as verified in Chapter **3.1**, the immersed specimens revealed a decreased ductility. Thus, the Young's moduli should increase with the immersion days. However, the Young's moduli increase cannot be a function of seawater concentration as it would generate an unrealistic stress concentration in between the affected and non-affected zones by seawater. Therefore, Young's moduli increase will be a function of the normalized Fick's law.

Regarding the water absorption, the prediction was made using Fick's law (see Eq. (**2.34**, Eq. **(2.35)** and Eq. **(2.36)**), is represented in **Figure 3.7** and the applied parameters are listed in **Table 3.5**. Since only two data points were available (at 229 and 900 days of immersion), the maximum amount of seawater absorption M_∞ was assumed to be at day 900. This assumption takes place because between 229 and 900 days of immersion, the difference in mass gain was slight, meaning that the specimen was very likely saturated between that time. It is difficult to know exactly when the specimen got saturated. Still, this assumption does not seem inappropriate because of the last section of Fick's law, where the mass gain remains approximately constant.

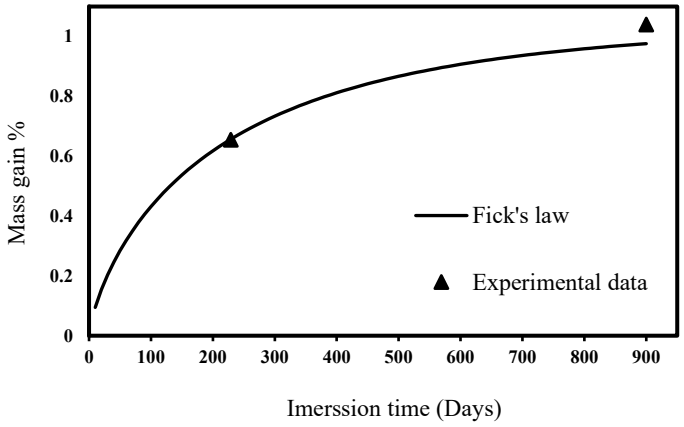

Figure 3.7. Application of the Fick's law for predicting the seawater absorption.

Table 3.5. Parameters of water absorption behavior for the application of Fick's law.

Saturation absorption M_∞ (%)	Slope k ($\times 10^{-5}d$)	Thickness h (mm)	Mass diffusivity coefficient D ($\times 10^{-8}\ mm^2/d$)
1.04	14.35	2.3	2.31

3.2.2.1. Implementation of Fick's law

The main objective of this section is to explain how Fick's first diffusion law was implemented in the user sub-routine. The diffusion distance and the wet volume[2] relation is fundamental to applying Fick's law in the user sub-routine.

Since diffusion is a complex phenomenon, the following assumptions were made:

- On day 900, the specimen is saturated, meaning the diffusion must reach all the integration points;
- It was considered that the diffusion only develops on the surfaces that have been cut, i.e., the surfaces B1 and B2[3] represented in **Figure 3.8**, are impermeable;

[2] Specimen's volume affected by the seawater diffusion.
[3] The opposite surface to B1. All surface's identification indexes denote the analogous.

- Because of the laminate's anisotropy, it should have different diffusion properties in different directions; however, the laminate was considered isotropic for this purpose;
- The diffusion process is identical on all permeable surfaces.
- The relation between the wet volume and the weight gain is linearly proportional.

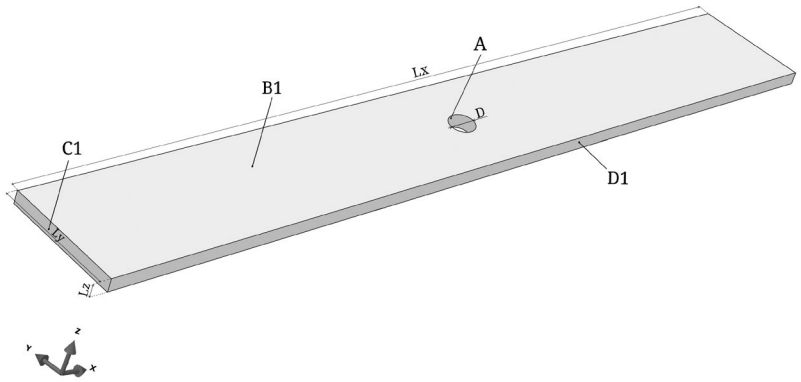

Figure 3.8. Identification of the specimen's surfaces and dimensions.

The functions of the diffusion distance to origin[4], situated in the center of surface B2, of each permeable surface[5], are shown in Equations **(3.1)**-**(3.5)**:

$$D_{C1distOrigin}(t) = -\frac{L_x}{2} + D_{dist}(t) \tag{3.1}$$

$$D_{C2distOrigin}(t) = \frac{L_x}{2} - D_{dist}(t) \tag{3.2}$$

$$D_{D1distOrigin}(t) = -\frac{L_y}{2} + D_{dist}(t) \tag{3.3}$$

$$D_{D2distOrigin}(t) = \frac{L_y}{2} + D_{dist}(t) \tag{3.4}$$

$$D_{AdistOrigin}(t) = D + D_{dist}(t) \tag{3.5}$$

$$D_{dist}(t) = A(t) \times \frac{L_y}{2} \tag{3.6}$$

The chosen function for A(t) must be able to replicate Fick's law in the user sub-routine. Figure 3.9 shows the path used to connect Fick's law and the only parameter that

[4] The reference axis to the Gauss points.
[5] Surfaces C1, C2, D1, D2, and A.

can be controlled in the UMAT, A(t). Fick's law relates the weight gain with immersion time; however, inserting weight into the analysis would produce immense complexities. Therefore, the assumed linear proportional relation between the wet volume and the weight gain allows using the prediction of weight gain provided by Fick's law without creating a much more complex analysis. Effectively, this assumption means that if Fick's law predicts that the specimen gains 10% of its saturation weight, then 10 % of the specimen volume is wet. This assumption allows connecting Fick's law and the wet volume W_{volume} which is important since the comparison between the normalized Fick's law and normalized W_{volume} allows the function A(t) to be chosen.

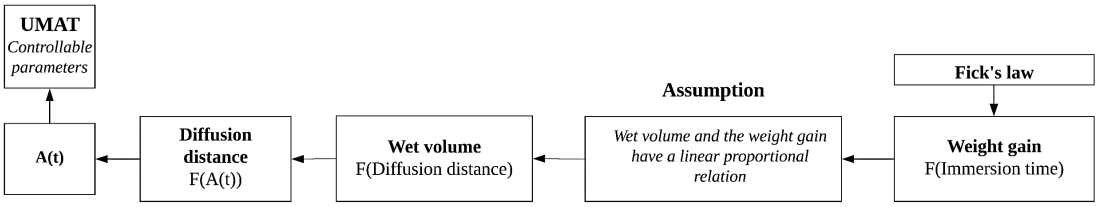

Figure 3.9. Relations for the implementation of Fick's law in the UMAT.

What allows connecting A(t) to the wet volume is the diffusion distance (Eq. **(3.6)**) since the wet volume is a function of the diffusion distance. Furthermore, the relation function between the diffusion distance and the W_{volume} is shown in Equation **(3.7)** and a detailed explanation of the equation's obtention can be found in Appendix C.

$$W_{volume}(D_{dist}) = 2L_z\, D_{dist}\{(L_y - 2D_{dist}) + (L_x)\} + L_z\pi\left(D_{dist} + \frac{D}{2}\right)^2 - L_z\pi\left(\frac{D}{2}\right)^2 - Sin\left[\frac{\pi}{2}\left(\frac{D_{dist}}{L_z/2}\right)^5\right] I_{vol} \quad (3.7)$$

where D_{dist} is the diffusion distance, L_x, L_y, L_z and D are the specimen's dimensions (see **Figure 3.8**), I_{vol} is a volume explained in Appendix C. The specimen is saturated when $W_{volume}(D_{dist}) =$ Specimen's volume; thus, because the diffusion kinematics are the same in all specimen's permeable surfaces, $W_{volume}(L_y/2) =$ Specimen's volume.

Figure 3.10 compares the normalized W_{volume}, using different functions for A(t), with the normalized Fick's law. As mentioned above, this comparison is crucial since now it is possible to find the most appropriate function for A(t).

The results show that the wet volume and immersion time relation is not linear when using a linear function for $A(t)$, as illustrated in **Figure 3.10**. As a result, the relation between the diffusion distance and the wet volume is not linear. However, when using $A(t)$=Normalized Fick's law, the average difference between the normalized Fick's law and the normalized wet volume is acceptable.

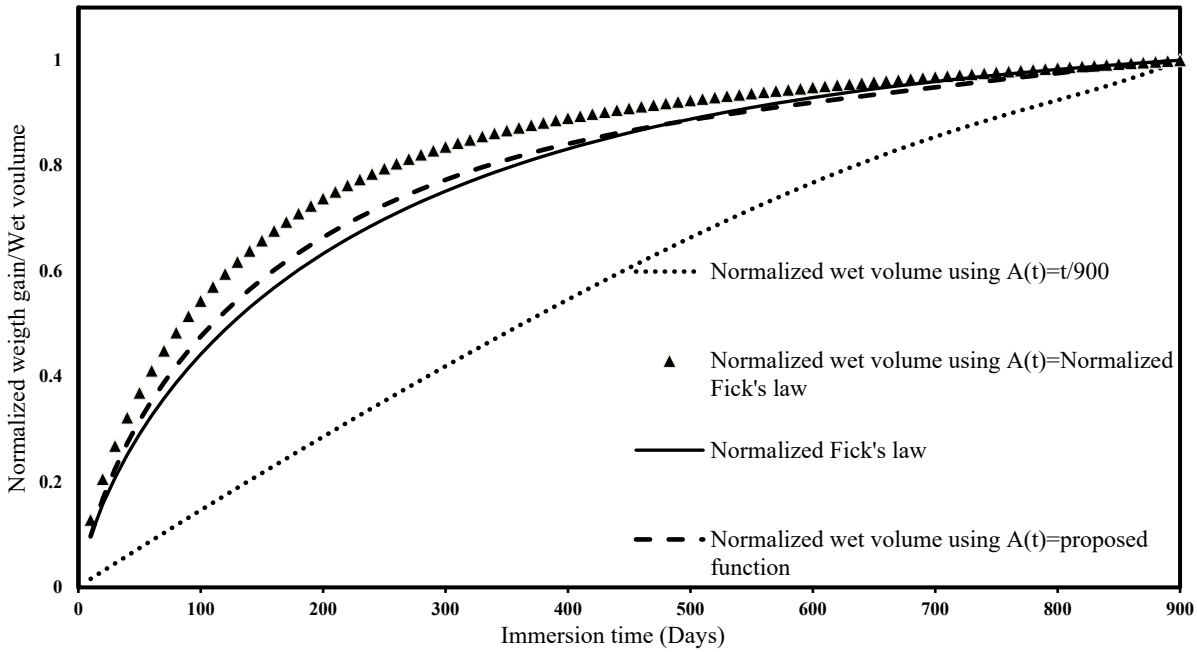

Figure 3.10. Comparison between the normalized wet volume, using different functions for A(t), and the normalized Fick's law.

Still, the error can be decreased using a correction function. Equation **(3.8)** combines the normalized Fick's law and a proposed fourth-order polynomial correction function. When applied to the normalized wet volume expression, the results show an average error of 2.5 % relative to the normalized Fick's Law. Hence, Equation **(3.8)** is adequate to reproduce Fick's law seawater weight gain prediction in the UMAT.

(3.8)

$$A(t) = \frac{M_\infty \left\{1 - exp\left[-7.3\left(\frac{D_{Coef} t \times 3600 \times 24}{{L_z}^2}\right)^{0.75}\right]\right\}}{M_{\infty f}} + 0.5(1 \times 10^{-12} t^4 - 3 \times 10^{-9} t^3 + 3 \times 10^{-6} t^2 - 9 \times 10^{-4} t - 0.0361$$

The above section explored how the diffusion distance of each permeable surface varies with the immersion time considering Fick's law. However, inside the wet volume, the seawater concentration is a function of time and diffusion distance since diffusion occurs in response to a concentration gradient, as **Figure 3.11** depicts.

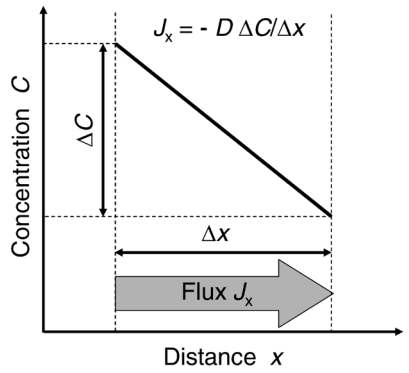

Figure 3.11. Illustration of Fick's first law, from [46].

Considering this concentration gradient in the analysis, it does not abolish the assumption between the wet volume and weight gain. The seawater concentration of 10% weight gain can vary relative to the diffusion surface in 10% of the specimen volume, and the relation between the wet volume and weight gain is still be considered proportionally linear. Therefore, the element's seawater concentration relative to its closer permeable surface C_{CS} is:

$$C_{CS} = 1 - \frac{D_{CS}}{D_{dist}} \tag{3.9}$$

where D_{CS} is the element's distance to its closer permeable surface.

3.2.2.2. Material properties modification

This section explains how the model predicts the strength reduction and stiffness increase, as verified in Chapter **3.1**. As stated before, prior research generally confirms that seawater damage is a function of seawater concentration in FRP. Hence, the strength will be a function of the seawater concentration, and can be defined as follows:

$$R_{\perp,\parallel}^{t,c} = R_{\perp,\parallel}^{t,c}(1 - kC_{CS}) \tag{3.10}$$

where k is an experimental curve fitting parameter.

Ideally, all the used specimen material properties should be known to apply the developed model with precision. However, since that data are not available, to reproduce the deformation that material experiences, it is necessary to use a fitting parameter A to modify the Young's modulus. The Equation **(3.11)** will modify the model's Young's modulus so it can have the same stress-strain behavior as the experimental model. Hence, the first term of the proposed function in Equation **(3.11)**, does not dependent on the immersion days, and will adapt the model's Young's modulus. Nevertheless, as it will be shown in Chapter 4, using all the other material properties from WWFE-II leads to good results. The second term of Equation **(3.11)** is to predict the increase of Young's modulus made by the seawater exposure. As mentioned before, unlike the reduction of strength, the increase of Young's modulus is a function of the normalized Fick's law, i.e:

$$E_i = E_{wwfe,i}A + E_{wwfe,i}N_{Fl}B \tag{3.11}$$

where $E_{wwfe,i}$ is the Young's modulus from WWFE-II, B is a fitting parameter, and N_{Fl} is the normalized Fick's law.

Both k and B are fundamental curve fitting parameters to ensure that the model works properly. However, parameter A is only required when the lamina properties are unknown; if the properties are known, then parameter A should equal one. Furthermore, the parameters k and B should be easily collected from a single experimental result.

4. RESULTS AND DISCUSSION

A numerical model for predicting the seawater damage in GFRP was developed, and within this chapter, the efficiency of the model is investigated. All the experimental curve fitting parameters used to implement the model are presented in **Table 4.1**.

Table 4.1. Strength and Young's moduli experimental curve fitting parameters.

Strength parameters	**Young's moduli parameters**	
k	A	B
0.26	0.55	0.45

The developed model main's methodology is to adapt the material properties considering Fick's law to replicate the real-world effects of seawater exposure. The lamina strengths are a function of the seawater concentration, and the Young's moduli are a direct function of Fick's law.

Firstly, the simulation results of the control specimen will be presented. The maximum principal deformation fields will be analyzed and discussed along with the damage progression in the specimen. Then, it will be reviewed the simulation of the specimen's mechanical behavior to evaluate the precision of Puck's criterion.

Secondly, the seawater damage model predictions for the seawater concentration in the specimen are shown, and the simulation results of the tensile strength tests are compared with the experimental data.

Thirdly, it will be presented the model's ability to predict the critical surfaces and where to modify the protective coatings of composite structures in order to, so it sustain higher loads in marine environments.

Lastly, mesh dependence and the duration of the simulations will be debated.

4.1. Control specimen

This section features comparisons between the experimental results and the numerical model for the control specimens (dry specimens, i.e. not immersed in seawater). The focus of this section is on the evaluation of Puck's failure criterion.

4.1.1. Maximum principal strain

Gonçalves [42] performed three, non-destructive tensile tests to confirm that the strain was linearly increasing with the load. The strain was measured with Digital Image Correlation (DIC). After implementing Puck's failure model, three simulations were also performed to compare the numerical principal strain fields with those obtained in each non-destructive tensile test.

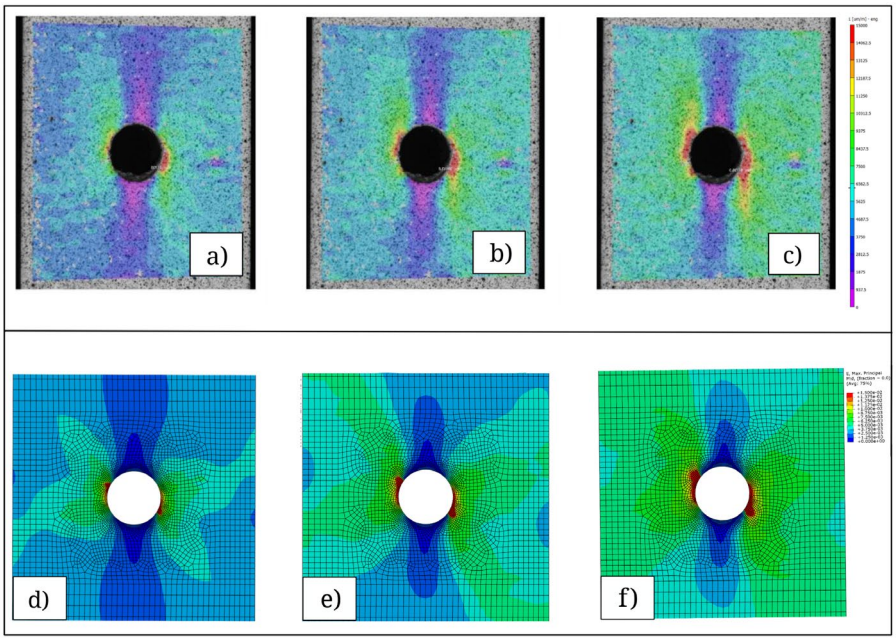

Figure 4.1. Comparison between the specimen's principal strain field obtained with DIC and ABAQUS Images a, b and c correspond to DIC results, and the remaining ones to ABAQUS with the application of Puck's failure theory; the images a-d, b- e and c-f correspond to loads of 4.3 kN, 4.875 kN and 5.5 kN, respectively.

As depicted in **Figure 4.1**, the numerical simulations and experimental results showed good agreement for the pattern distribution of principal strain. Indeed, when comparing DIC to the implemented Puck's failure model, the strain profile is similar for the three loading levels, which is an interesting outcome. Furthermore, although the loading was uniformly applied in the external surfaces, as described in Section **3.1**, the experimental results show that the principal strain field is not symmetric, and Puck's failure theory can also predict the asymmetry. The specimen revealed a different behavior when applying lower loads, and **Figure 4.2** can help to understand what causes the asymmetry.

At 3.0 kN or lower, no matrix damage occurs at the surface[6] and no asymmetry is perceptible in the strain field. As the load increases, matrix damage starts to build up, and the strain asymmetry is lightly perceptible. At 5.0 kN or higher, a pronounced asymmetrical matrix damage pattern occurs, generating the uneven strain pattern that is verified in the experiments. The asymmetry is presumed to occur due to the lamina sequence in the laminate.

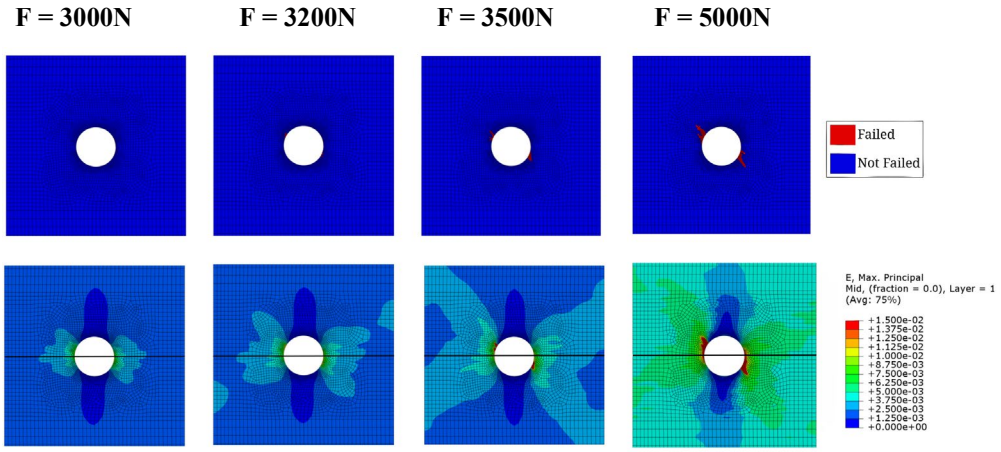

Figure 4.2. Puck's matrix damage and maximum principal deformation pattern progression.

4.1.2. Load-Displacement plot

The load-displacement plots determined numerically and that obtained in the experiments are shown in **Figure 4.3**. At this point, since no water effect is concerned, the prediction only reflects the implementation of Puck's failure theory. In all simulations, the final failure is assumed to occur when the fiber failure crosses all the specimen width, accompanied by a sudden escalation of the displacement. The model predicts the failure load with an error of 5.1% and the displacement at failure with an error of 13.7 % compared with the average experimental results presented in **Table 3.1**.

[6] Except as otherwise indicated, all the figures showing deformation fields and damage represent the first ply of the laminate, i.e., the surface ply with the fibers in the x-axis direction.

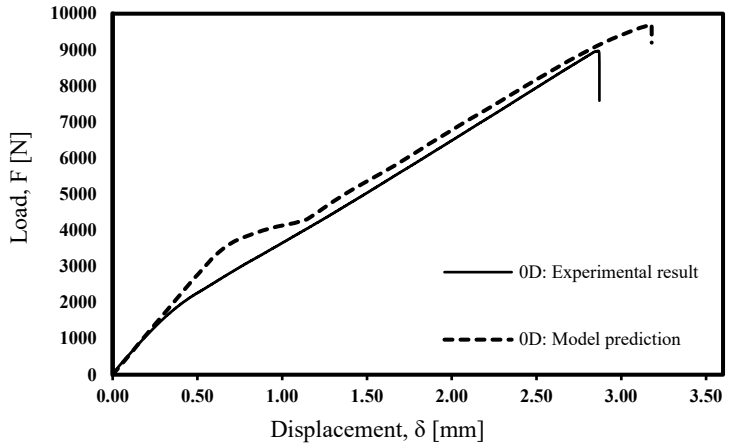

Figure 4.3. Load vs. displacement plot. Comparison between the experimental data and the model prediction for the control specimen.

Even though the model could predict the final values with reasonable precision, the load vs. displacement plot exhibits a non-linear behavior following the initial linear behavior at approximately 3.1 kN. Although there is a slight non-linearity on the experimental curve, it is noticed a disagreement between the experimental data and the numerical predictions. Nevertheless, this is a complex behavior to predict because the deformation is dominated by non-linear behavior in a multi-layer laminate. Moreover, neither of the failure theories tested in the failure exercises made by Soden et al. [47] covered this phenomenon correctly.

The aggressive non-linear behavior is caused by the non-catastrophic matrix failure, happening in all 90º and 45º plies. **Figure 4.4** illustrates the Inter Fiber Failure (IFF) pattern progression in ply 12 (90º) in the center zone of the specimen. When the load reaches approximately 3.5 kN, the IFF covers most of the width of the specimen's center zone. The damaged layers cannot be directly stressed in tension, but compressive and shear stresses can still be transmitted due to contact and friction. In fact, the IFF leads to a tension redistribution within the laminate as detailed in Chapter **2.2.2**.

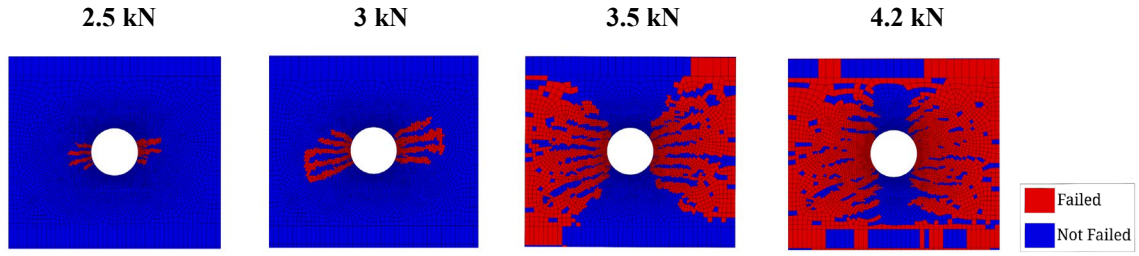

Figure 4.4. IFF pattern progression at the 12 ply (90º) for control specimens.

Figure 4.5 compares the linear strain ε_{11} of 12 nodes, one for each ply, situated in the same z-axis position, for three load levels. It can be verified that the 0º plies are notably more deformed than the others, which indicates that load is transferred mainly by those plies.

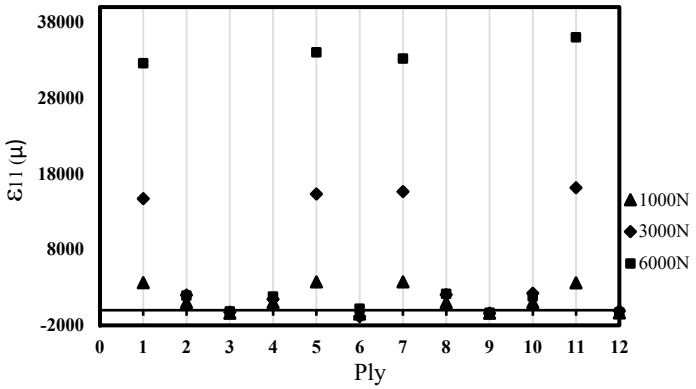

Figure 4.5. Linear strain ε_{11} of the 12 plies in same z-axis position at different loads.

4.1.3. Damage development

In terms of the damage development, the hole's borderline is where the crack starts to spread, as verified by Gonçalves [42] in the fatigue testing. **Figure 4.6** and **Figure 4.7** depict the matrix and fiber damage progression at the 7.0 kN, 8.0 kN, 9.0 kN , and 9.7 kN, respectively. The matrix failure antecedes the failure in the fiber as expected. The matrix damage asymmetry at 5.0 kN, verified above in **Figure 4.2**, expanded. It can be observed at 8.0 kN that, as the load increased and the fiber damage developed, the matrix damage exhibited a rapid growth. At 9.0 kN, the matrix damage covered all the width and thickness in the middle of the specimen.

Regarding the fiber failure, it only took place on the 0º plies since the others pliers' fibers are not being requested. At about 7.0 kN, the fiber damage appeared and, then, as the

load increased, it propagated along a 90º angle relative to the loading direction. At last, the test specimen was fully fractured under approximately 9.7 kN. The failed region induced by IFF is much wider than that induced by FF.

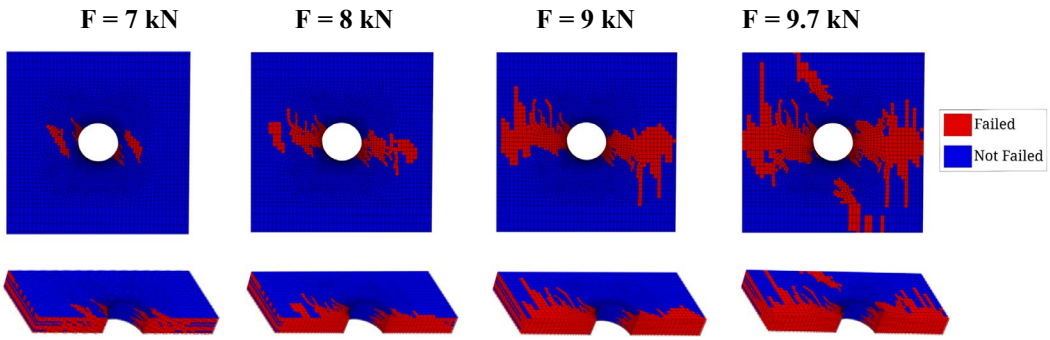

Figure 4.6. IFF pattern progression prediction.

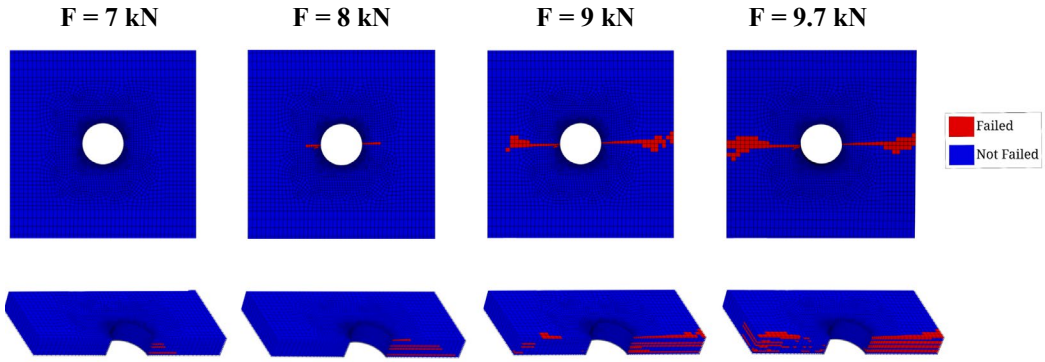

Figure 4.7. FF pattern progression prediction.

4.2. Seawater exposure damage model

4.2.1. Seawater concentration prediction

Figure 4.8 illustrates de prediction of seawater concentration after 30, 60, 150, 400, and 900 immersion days. With the increase of the immersion days, the diffusion distance increases, causing the diffused regions to cover the specimen's volume to a greater extent.

The concentration distribution is identical from day 400 to 900, even though 300 days later. This result is expected since the weight gain in the last section of Fick's law remains approximately constant.

After 900 days of immersion, since the specimen is considered saturated, the distribution of the seawater concentration remains equal to day 900.

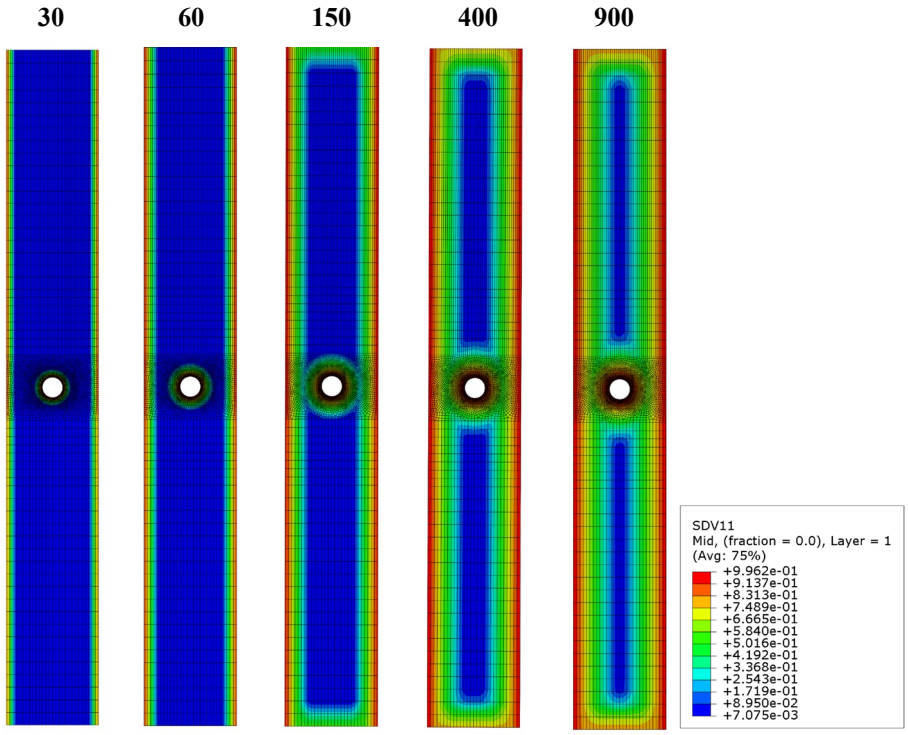

Figure 4.8. Model prediction of the concentration of seawater in the specimen after 30, 60, 150, 400 and 900 days of immersion.

Figure 4.9 exhibits the model prediction of lamina's tensile strength in the fiber direction $R_{||}^{t}$ distribution after 400 immersion days. As anticipated, it is verified a reverse distribution compared to the seawater concentration. The closer an element is to a permeable surface, the lower its tensile strength is; thus, the elements in remoter positions have higher tensile strength. It is important to point out that the hole's border zone, where the fiber failure initiates, also has reduced tensile strength.

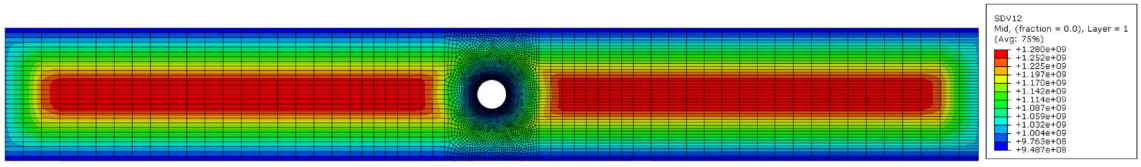

Figure 4.9. Prediction of lamina's tensile strength in fiber direction distribution after 400 days of immersion.

4.2.2. Prediction of the mechanical behavior

Figure 4.10 shows the load-displacement plots obtained experimentally and simulated numerically for 0 and 900 immersion days.

The model predicts the failure load with an error of 4% and the displacement at failure with an error of 25% compared to the average values presented in **Table 3.2**. The displacement at failure error is not significant considering the high standard deviation of the data for the displacement.

The model accurately predicts the laminate's behavior after the, already mentioned, initial behavior. The initial aggressive non-linear behavior of the curve is softened with the decrease in the material's ductility.

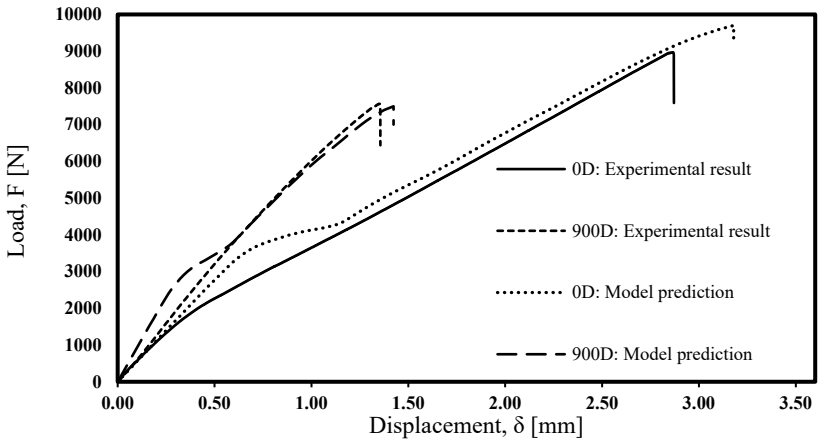

Figure 4.10. Load-displacement plot: experimental results and prediction of the effects of the seawater exposure for 0 and 900 immersion days.

Figure 4.11 shows the load vs. displacement plots predicted with the proposed model for different immersion days. Most of the strength and ductility loss occurs in the first days of immersion. The difference between the specimen's immersion for 120 and 900 days is insignificant. Since most of the water absorption occurs in the first months of immersion, most of the damage also occurs in that period. This result agrees with the study made in 1987 by Pritchard et. at. [37] and shown in Chapter **2.5.2**, where it was proved that the damage in

the composite is a function of the water concentration, and after saturation, no more damage seems to occur.

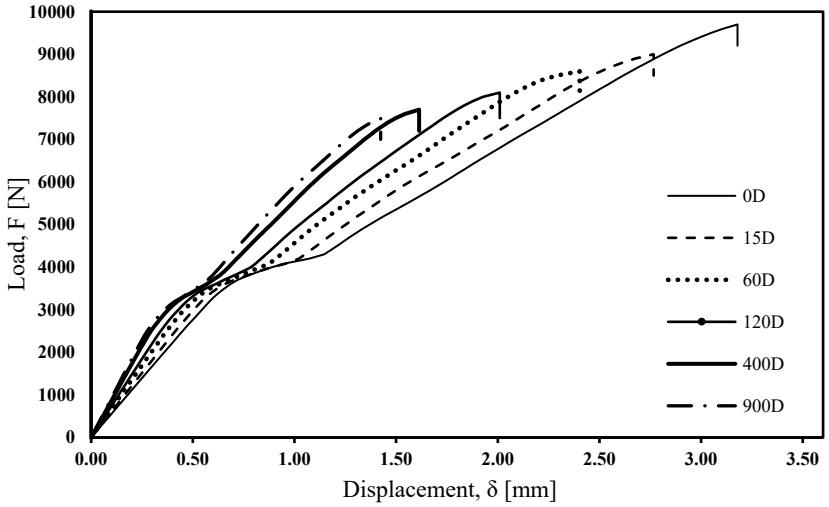

Figure 4.11. Load-displacement plot: prediction of the effects of the seawater exposure for different immersion days.

Figure 4.12 shows the model prediction for the failure load vs. the immersion days. It can be observed that most of the damage occurs in the first three months of immersion, and after approximately 250 days, no significant change occurs in the failure load. The following equation was obtained via nonlinear regression and describes the failure load vs. immersion days (ID).

$$L[N] = 9862.19(1 + ID)^{-0.04029} \tag{4.1}$$

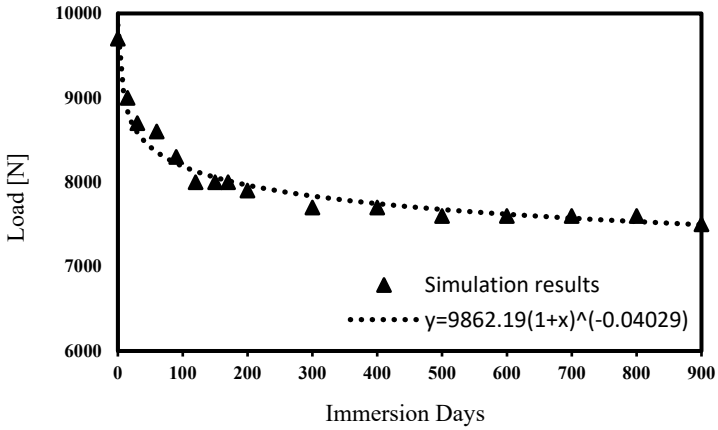

Figure 4.12. Model prediction of the failure load vs. immersion days

4.2.3. Identification of critical surfaces

Until now, it was assumed that the hole's surface and surfaces D1 and D2 were permeable so that the seawater could penetrate into the specimen through those surfaces. However, it would be interesting to understand how the specimen would behave with different impermeable surfaces. **Figure 4.13** illustrates the comparison between the seawater concentration with an impermeable hole surface and a permeable hole surface.

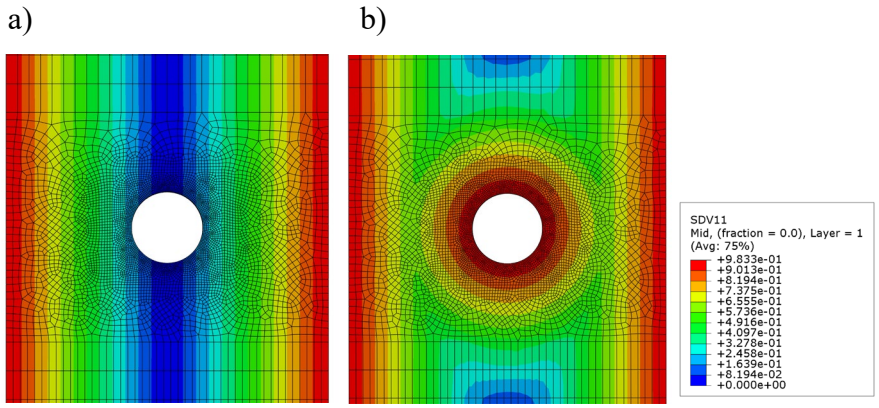

Figure 4.13. Seawater concentration with: a) impermeable hole surface; b) permeable hole surface.

Figure 4.14 compares the specimen's behavior in the case of the non-permeability of the surfaces D1 and D2, and the hole's surface. In the case of surfaces D1 and D2 being simultaneously impermeable, the difference in failure load is irrelevant. However, the model

predicts that the specimen could sustain 13 % more load in the case of a non-permeable hole. This is a coherent result since a stress concentration is verified in the hole's borderline zone.

Thus, an efficient way to improve the specimen's strength in a marine environment would be to focus the application of protective coatings on the hole's surface.

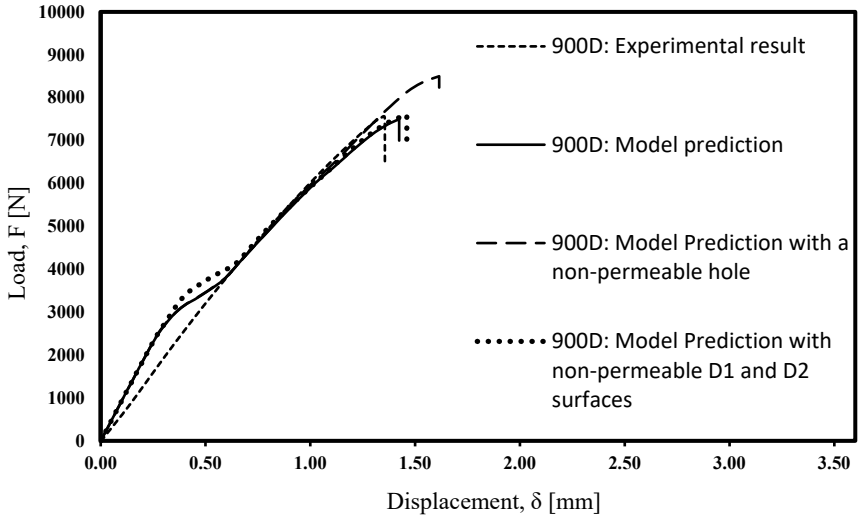

Figure 4.14. Model prediction of the failure load in the case of different non-permeable surfaces.

4.3. Mesh dependence and simulation duration study

Multiple simulations were run to understand how the mesh quality affected the simulation results. All simulations were performed for a 900-day immersion scenario. The study consisted in changing the mesh size of two regions: the specimen's center region close to the hole; and the additional regions. **Table 4.2** summarizes the parameters used in the mesh dependence studies and results of those studies. The mesh size location 1 and 2 concern the hole's borderline, and a close region around the hole, respectively. Locations 3 and 4 concern the specimen's length[7] and width[8], respectively. The simulation 2 represents the mesh used in all simulations of the present work.

[7] X-axis direction.
[8] Y-axis direction.

Table 4.2. Mesh dependence parameters and results.

Variables	Simulation		
	1	**2**	**3**
Mesh size in location 1 (mm)	0.05	**0.05**	0.03
Mesh size in location 2 (mm)	0. 5	**0. 5**	0. 3
Mesh size in location 3 (mm)	1	**1**	1
Mesh size in location 4 (mm)	3	**1**	1
Element count	57232	**102614**	201229
Node count	69412	**124046**	239000
Failure Load (N)	7400	**7400**	7400
Displacement at failure (mm)	1.69	**1.65**	1.60

Results show that displacement at failure is considerably mesh-dependent. With 2.7 times more elements relative to simulation 2, 12% more displacement was observed. With this element number, the simulation time increased significantly. Furthermore, even if convergency was reached with a considerably high number of elements, because of the amount of simulation required to find the fitting parameters and to simulate numerous scenarios presented in this dissertation, the converged mesh could not be utilized. Regarding the load at failure, it did not suffer any changes over approximately 40 000 elements. This result would probably not be verified in the case of a structure without a stress concentration zone, as verified in the analyzed specimen.

Figure 4.15 shows the relation between the simulation time and the number of elements. An exponential relationship between both variables was found which agrees with the discussion presented in Chapter **2.6**. This relation between simulation time and the number of elements verified in quasi-static analysis causes complications when searching for mesh convergence, as verified above.

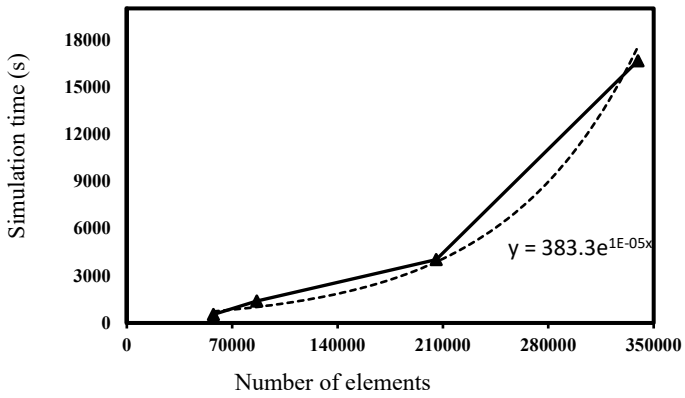

Figure 4.15. Relation between simulation time and number of elements.

5. CONCLUSIONS AND PROPOSALS FOR FUTURE RESEARCH

5.1. Conclusions

The work developed within the scope of this dissertation focused on creating a unique model capable of predicting the seawater exposure effects on glass fiber-reinforced polymers. The developed model contributes to the research of hostile environment effects in composite materials. If further validated, this model can be an important tool for composite structural engineers since it helps to understand how to modify a composite structure to sustain higher loads in marine environments.

The main conclusions of the developed work are:

- The model predicted the failure load with exceptional precision and the displacement at failure with acceptable precision;
- Regarding material behavior, the model presented a nonrealistic non-linear behavior in the load-displacement plot. This behavior has already been verified in other studies where Puck's failure theory was implemented. Still, this behavior only occurred in the early stage of the loading process; after a certain load level, the model presents the same behavior verified in the experimental tests;
- The model could predict the critical surfaces to modify in order to improve the mechanical behavior and, thus, sustain higher loads in a marine environment;
- The failure load is not particularly mesh-dependent; convergency is achieved with a reasonable mesh size in the center of the specimen. However, the displacement is considerably mesh-dependent. The utilized mesh results differ slightly from those obtained with finer meshes;
- Convergency in terms of displacement was not achieved by reducing the mesh in different specimen zones. Because of the proven exponential relationship between the number of elements and the simulation time, above approximately 700,000

elements, the simulation required more than one day to complete. This made the search for convergence impractical;

- The model is not simple to implement if the analyzed structure has a complex geometry because it is necessary to manually identify all permeable surfaces and calculate the diffusion distance for each one relative to the origin.

5.2. Future projects

A solution for determining the seawater effects on the resistance of GFRP was developed; most structures, however, fail not because of the application of a single, static load but because of the cumulative and unrecoverable damage done by multiple consecutive loadings. Therefore, the developed model could be tested in a progressive fatigue damage model (PFDM) like, for example, the one developed by Shorkrieh et al. [48].

Also, the developed model must be evaluated in different conditions in order to explore its potentialities and limitations. This can be achieved using different laminate layouts, executing different strength tests, using different geometries, and more frequent data.

Finally, this model was developed using Puck's failure criterion. Despite the good results and the fact that Puck's failure criterion is remarkable, using the model with another failure criterion like the Tsai-Hill failure criterion would be interesting.

REFERENCES

[1] A. Ben Soussia, A. Mkaddem, and M. El Mansori, "Rigorous treatment of dry cutting of FRP – Interface consumption concept: A review," *Int. J. Mech. Sci.*, vol. 83, pp. 1–29, Jun. 2014, doi: 10.1016/J.IJMECSCI.2014.03.017.

[2] C. W. Cable, "The Effect of Defects in Glass-Reinforced Plastic (GRP)," *Mar. Technol. SNAME News*, vol. 28, no. 02, pp. 91–98, Mar. 1991, doi: 10.5957/MT1.1991.28.2.91.

[3] A. R. Bunsell and J. Renard, *Fundamentals of fibre reinforced composite materials*, 1st Editio. 2022.

[4] Y. Rajapakse and P. Davies, *Durability of Composites in a Marine Environment*, vol. 208. Dordrecht: Springer Netherlands, 2014. doi: 10.1007/978-94-007-7417-9.

[5] Z. Hashin, "Failure Criteria for Unidirectional Fiber Composites," *J. Appl. Mech.*, vol. 47, no. 2, pp. 329–334, Jun. 1980, doi: 10.1115/1.3153664.

[6] M. J. Hinton, A. S. Kaddour, and P. D. Soden, "A comparison of the predictive capabilities of current failure theories for composite laminates, judged against experimental evidence," *Compos. Sci. Technol.*, vol. 62, no. 12–13, pp. 1725–1797, Sep. 2002, doi: 10.1016/S0266-3538(02)00125-2.

[7] R. Talreja and C. V. Singh, "Damage and failure of composite materials," *Damage Fail. Compos. Mater.*, pp. 1–304, Jan. 2012, doi: 10.1017/CBO9781139016063.

[8] J. Varna, R. Joffe, N. V. Akshantala, and R. Talreja, "Damage in composite laminates with off-axis plies," *Compos. Sci. Technol.*, vol. 59, no. 14, pp. 2139–2147, Nov. 1999, doi: 10.1016/S0266-3538(99)00070-6.

[9] M. Knops, "Analysis of failure in fiber polymer laminates: The theory of alfred puck," *Anal. Fail. Fiber Polym. Laminates Theory Alfred Puck*, pp. 1–205, 2008, doi: 10.1007/978-3-540-75765-8.

[10] H. M. Deuschle, "3D Failure Analysis of UD Fibre Reinforced Composites: Puck's Theory within FEA," UNIVERSITÄT STUTTGART, 2010.

[11] E. K. Gamstedt and B. A. Sjögren, "Micromechanisms in tension-compression fatigue of composite laminates containing transverse plies," *Compos. Sci. Technol.*, vol. 59, no. 2, pp. 167–178, Feb. 1999, doi: 10.1016/S0266-3538(98)00061-X.

[12] H. M. Deuschle and A. Puck, "Application of the Puck failure theory for fibre-reinforced composites under three-dimensional stress: Comparison with experimental results:," *http://dx.doi.org/10.1177/0021998312462158*, vol. 47, no. 6–7, pp. 827–846, Mar. 2013, doi: 10.1177/0021998312462158.

[13] W. J. G. Choi N S, Kinloch A J, "Delamination fracture of multidirectional carbon-fiber / epoxy composites under mode I, mode II and mixed mode I/II loading," *J. Compos. Mater.*, pp. 73–100, 1999.

[14] I. M. Daniel and I. Ori, *Engineering Mechanics of Composite Materials*, Second Edi. 2006.

[15] E. Carrera, "Mixed layer-wise models for multilayered plates analysis," *Compos. Struct.*, vol. 43, no. 1, pp. 57–70, 1998, doi: 10.1016/S0263-8223(98)00097-X.

[16] S. Abrate and M. Di Sciuva, "Equivalent single layer theories for composite and sandwich structures: A review," *Compos. Struct.*, vol. 179, pp. 482–494, Nov. 2017, doi: 10.1016/J.COMPSTRUCT.2017.07.090.

[17] J. N. Reddy and D. H. Bobbins, "Theories and Computational Models for Composite Laminates," *Appl. Mech. Rev.*, vol. 47, no. 6, pp. 147–169, Jun. 1994, doi: 10.1115/1.3111076.

[18] A. Inc., *ABAQUS Analysis User's manual*, V6.61. 2006.

[19] Y. Guo, A. P. Nagy, and Z. Gürdal, "A layerwise theory for laminated composites in the framework of isogeometric analysis," *Compos. Struct.*, vol. 107, pp. 447–457, Jan. 2014, doi: 10.1016/J.COMPSTRUCT.2013.08.016.

[20] G. C. Kahandawa, J. Epaarachchi, H. Wang, and K. T. Lau, "Use of FBG

sensors for SHM in aerospace structures," *Photonic Sensors*, vol. 2, no. 3, pp. 203–214, Sep. 2012, doi: 10.1007/S13320-012-0065-4.

[21] G. Kress, "Examination of Hashin's failure criteria for the second world-wide failure exercise," *J. Compos. Mater.*, vol. 46, no. 19–20, pp. 2539–2561, Sep. 2012, doi: 10.1177/0021998312449892.

[22] M. J. H. A S Kaddoura, S. Lic, and and P A Smithd, "The world-wide failure exercises: How can composite design and manufacture communities build their strength," *Eur. Conf. Compos. Mater.*, 2014.

[23] J. Gu and P. Chen, "Extension of Puck's inter fibre fracture (IFF) criteria for UD composites," *Compos. Sci. Technol.*, vol. 162, pp. 79–85, Jul. 2018, doi: 10.1016/J.COMPSCITECH.2018.04.019.

[24] M. A. Neto, A. Amaro, R. Luis, J. Cirne, and R. Leal, "Engineering computation of structures: The finite element method," *Eng. Comput. Struct. Finite Elem. Method*, pp. 1–310, Jan. 2015, doi: 10.1007/978-3-319-17710-6/COVER.

[25] C. S. Lee, J. H. Kim, S. K. Kim, D. M. Ryu, and J. M. Lee, "Initial and progressive failure analyses for composite laminates using Puck failure criterion and damage-coupled finite element method," *Compos. Struct.*, vol. 121, pp. 406–419, Mar. 2015, doi: 10.1016/J.COMPSTRUCT.2014.11.011.

[26] A. Puck, J. Kopp, and M. Knops, "Guidelines for the determination of the parameters in Puck's action plane strength criterion," *Compos. Sci. Technol.*, vol. 62, no. 3, pp. 371–378, 2002, doi: 10.1016/S0266-3538(01)00202-0.

[27] G. Lutz, "The Puck theory of failure in laminates in the context of the new guideline," Herne, Germany, 2014.

[28] H. M. Deuschle and A. Puck, "Application of the Puck failure theory for fibre-reinforced composites under three-dimensional stress: Comparison with experimental results:," *http://dx.doi.org/10.1177/0021998312462158*, vol. 47, no. 6–7, pp. 827–846, Mar. 2013, doi: 10.1177/0021998312462158.

[29] G. Maymon, R. Briley, and L. Rehfield, "Influence of Moisture Absorption and Elevated Temperature on the Dynamic Behavior of Resin Matrix Composites:

Preliminary Results," *Adv. Compos. Mater. Eff.*, pp. 221-221–13, Mar. 2009, doi: 10.1520/STP34866S.

[30] A. G. Andreopoulos and P. A. Tarantili, "Water sorption characteristics of epoxy resin–UHMPE fibers composites," *J. Appl. Polym. Sci.*, vol. 70, no. 4, pp. 747–755, 1998, doi: https://doi.org/10.1002/(SICI)1097-4628(19981024)70:4<747::AID-APP14>3.0.CO;2-U.

[31] A. Pavan, P. Dayananda, K. M. Vijaya, S. Hegde, and P. Narampady Hosagade, "Influence of seawater absorption on vibrational and tensile characteristics of quasi-isotropic glass/epoxy composites," *J. Mater. Res. Technol.*, vol. 8, no. 1, pp. 1427–1433, Jan. 2019, doi: 10.1016/J.JMRT.2018.10.008.

[32] J. L. Thomason, "The interface region in glass fibre-reinforced epoxy resin composites: 2. Water absorption, voids and the interface," *Composites*, vol. 26, no. 7, pp. 477–485, Jul. 1995, doi: 10.1016/0010-4361(95)96805-G.

[33] L. Bian, J. Xiao, J. Zeng, and S. Xing, "Effects of seawater immersion on water absorption and mechanical properties of GFRP composites:," *http://dx.doi.org/10.1177/0021998312436992*, vol. 46, no. 25, pp. 3151–3162, Feb. 2012, doi: 10.1177/0021998312436992.

[34] C.-H. Shen and G. S. Springer, "Moisture Absorption and Desorption of Composite Materials".

[35] J. Comyn, Ed., "Polymer Permeability," 1985, doi: 10.1007/978-94-009-4858-7.

[36] J. U. N. Wang, H. O. T. A. Gangarao, R. Liang, and W. Liu, "Durability and prediction models of fiber-reinforced polymer composites under various environmental conditions: A critical review:," *http://dx.doi.org/10.1177/0731684415610920*, vol. 35, no. 3, pp. 179–211, Nov. 2015, doi: 10.1177/0731684415610920.

[37] G. Pritchard and S. D. Speake, "The use of water absorption kinetic data to predict laminate property changes," *Composites*, vol. 18, no. 3, pp. 227–232, Jul. 1987, doi: 10.1016/0010-4361(87)90412-5.

[38] H. Saadatmanesh and F. E. Tannous, "Environmental Effects on the Mechanical

Properties of E-Glass FRP Rebars," *ACI Mater. J.*, p. 9, 1998, Accessed: May 16, 2022. [Online]. Available: https://www.academia.edu/77515489/Environmental_Effects_on_the_Mechanical_Properties_of_E_Glass_FRP_Rebars

[39] E. P. Gellert and D. M. Turley, "Seawater immersion ageing of glass-fibre reinforced polymer laminates for marine applications," *Compos. Part A Appl. Sci. Manuf.*, vol. 30, no. 11, pp. 1259–1265, 1999, doi: 10.1016/S1359-835X(99)00037-8.

[40] M. C. C. Oliveira, "Algoritmos e estratégias de gestão do problema de contacto com atrito em grandes deformações: aplicação à estampagem de chapas metálicas," Dissertação para Doutoramento em Ciências da Engenharia Mecânica, Faculdade de Ciências e Tecnologia da Universidade de Coimbra, 2005.

[41] A. E. Tekkaya, "State-of-the-art of simulation of sheet metal forming," *J. Mater. Process. Technol.*, vol. 103, no. 1, pp. 14–22, Jun. 2000, doi: 10.1016/S0924-0136(00)00413-1.

[42] C. Gonçalves, "Efeito de ambientes hostis na resposta à fadiga de laminados vidro/epóxido," Dissertação de Mestrado, Faculdade de Ciências e Tecnologia da Universidade de Coimbra, 2019.

[43] R. dos S. Jorge, "Análise do estado de deformação em laminados vidro/epóxido imersos em água salgada sujeitos a cargas cíclicas," Dissertação de Mestrado, Faculdade de Ciências e Tecnologia da Universidade de Coimbra, 2021.

[44] D. M. de C. Aguiar, "Efeito do tempo de imersão em ambiente salino na resposta à fadiga de laminados vidro/epóxido.," Faculdade de Ciências e Tecnologia da Universidade de Coimbra, 2021.

[45] J. M. K. Ted Belytschko, Jame Shau-Jen ONG, Wing Kam LIU, "Hourglass control in linear and nonlinear problems," *Comput. Methods Appl. Mech. Eng.*, vol. 43, pp. 251–276, 1983.

[46] H. Mehrer, *Diffusion in Solids*, vol. 155. Berlin, Heidelberg: Springer Berlin

Heidelberg, 2007. doi: 10.1007/978-3-540-71488-0.

[47] P. D. Soden, M. J. Hinton, and A. S. Kaddour, “Biaxial test results for strength and deformation of a range of E-glass and carbon fibre reinforced composite laminates: failure exercise benchmark data,” *Compos. Sci. Technol.*, vol. 62, no. 12–13, pp. 1489–1514, Sep. 2002, doi: 10.1016/S0266-3538(02)00093-3.

[48] M. M. Shokrieh and L. B. Lessard, “Progressive Fatigue Damage Modeling of Composite Materials, Part I: Modeling:,” *http://dx.doi.org/10.1177/002199830003401301*, vol. 34, no. 13, pp. 1056–1080, Jul. 2016, doi: 10.1177/002199830003401301.

APPENDIX A-MECHANICAL PROPERTIES FROM THE WWFE-II

Fibre type	IM7	T300	A-S	S2-glass	E-Glass
Matrix	8551-7	PR-319	Epoxy1	Epoxy2	MY750
Fibre volume fraction V_f (%)	60	60	60	60	60
Longitudinal modulus E_1 (GPa)	165*	129	140*	52	45.6
Transverse modulus E_2 (GPa)	8.4	5.6+	10	19	16.2
Through-thickness modulus E_3 (GPa)	8.4	5.6+	10	19	16.2
In-plane shear modulus G_{12} (GPa)	5.6*	1.33+	6*	6.7*	5.83*
Transverse shear modulus G_{13} (GPa)	5.6*	1.33+	6*	6.7*	5.83*
Through-thickness shear modulus G_{23} (GPa)	2.8	1.86	3.35	6.7	5.7
Major Poisson's ratio υ_{12}	0.34	0.318	0.3	0.3	0.278
Major transverse Poisson's ratio υ_{13}	0.34	0.318	0.3	0.3	0.278
Through-thickness Poisson's ratio υ_{23}	0.5	0.5	0.49	0.42	0.4
Longitudinal tensile strength X_T (MPa)	2560	1378	1990	1700	1280
Longitudinal compressive strength X_C (MPa)	1590	950	1500	1150	800
Transverse tensile strength Y_T (MPa)	73	40	38	63	40
Transverse compressive strength Y_C (MPa)	185**	125**	150**	180**	145**
Through-thickness tensile strength Z_T (MPa)	63	40	38	50	40
Through-thickness compressive strength Z_C (MPa)	185**	125**	150**	180**	145**
In-plane shear strength S_{12} (MPa)	90**	97**	70**	72**	73**
Transverse shear strength S_{13} (MPa)	90**	97**	70**	72**	73**
Through-thickness shear strength S_{23} (MPa)	57	45	50	40	50
Longitudinal tensile failure strain ε_{1T} (%)	1.551	1.07	1.42	3.27	2.807
Longitudinal compressive failure strain ε_{1C} (%)	1.1	0.74	1.2	2.21	1.754
Transverse tensile failure strain ε_{2T} (%)	0.87	0.43	0.38	0.33	0.246
Through-thickness compressive failure strain ε_{2C} (%)	3.2	2.8	1.6	1.5	1.2
Transverse tensile failure strain ε_{3T} (%)	0.755	0.43	0.38	0.263	0.246
Through-thickness compressive failure strain ε_{3C} (%)	3.2	2.8	1.6	1.5	1.2
In-plane shear failure strain γ_{12u} (%)	5	8.6	3.5	4	4
Transverse shear failure strain γ_{13u} (%)	5	8.6	3.5	4	4
Through-thickness shear failure strain γ_{23u} (%)	2.1	1.5	1.5	0.59	0.88
Longitudinal thermal coefficient α_1 (10^{-6}/°C)	-1	-1	-1	8.6	8.6
Transverse thermal coefficient α_2 (10^{-6}/°C)	18	26	26	26.4	26.4
Through-thickness thermal coefficient α_3 (10^{-6}/°C)	18	26	26	26.4	26.4
Stress free temperature (°C)	177	120	120	120	120

Figure 5.1. Mechanical properties for four unidirectional lamina, from [22]

Fibre type	IM7	T300	AS	S2-glass	E-Glass
Longitudinal modulus E_{f1} (GPa)	276	231	231	87	74
Transverse modulus E_{f2} (GPa)	19	15	15	87	74
Transverse modulus E_{f3} (GPa)	19	15	15	87	74
In-plane shear modulus G_{f12} (GPa)	27	15	15	36	30.8
Major Poisson's ratio υ_{f12}	0.2	0.2	0.2	0.2	0.2
Major Poisson's ratio υ_{f13}	0.2	0.2	0.2	0.2	0.2
Transverse shear modulus G_{f23} (GPa)	7	7	7	36	30.8
Longitudinal tensile strength X_{f1T} (MPa)	5180	2500	3500	2850	2150
Longitudinal compressive strength X_{f1C} (MPa)	3200	2000	3000	2450	1450
Longitudinal tensile failure strain ε_{f1T} (%)	1.87	1.086	1.515	3.27	2.905
Longitudinal compressive failure strain ε_{f1C} (%)	1.16	0.869	1.298	2.82	1.959
Longitudinal thermal coefficient α_{f1} (10^{-6}/°C)	-0.4	-0.7	-0.7	5	4.9
Transverse thermal coefficient α_{f2} (10^{-6}/°C)	5.6	12	12	5	4.9
Through-thickness thermal coefficient α_{f3} (10^{-6}/°C)	5.6	12	12	5	4.9

Figure 5.2. Mechanical properties of four fiber types, from [10].

APPENDIX B- SUBROUTINES WATERDAMAGE AND SEARCHFP

The subroutine *Waterdamage,* which has its flowchart represented in Figure 5.3, is called at each integration point to change or keep the material properties on each integration point. Firstly, it computes the diffusion distance with Equation (3.6). Then, it is necessary to compute the diffusion distance to the origin of each permeable surface so it is possible to verify if the current integration point is within the damaged zone. If it is, the seawater concentration is calculated based on the Equations (3.1)-(3.5) and the mechanical properties are adjusted based on it. Lastly, the properties are saved in state variables, so this routine is called only one time per simulation.

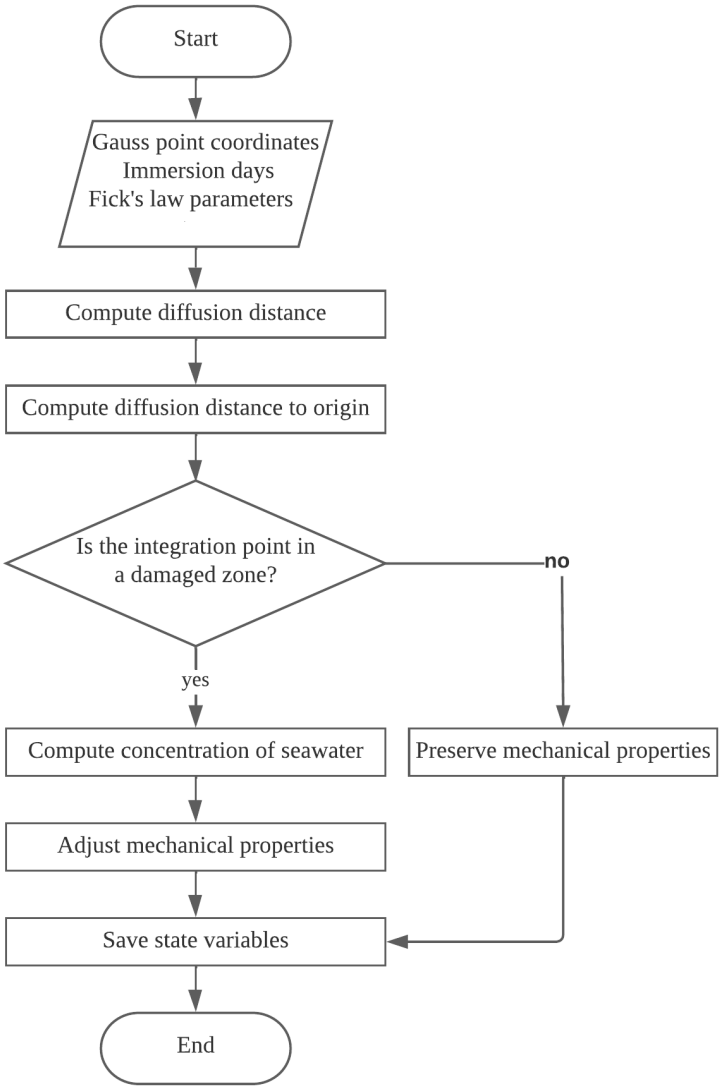

Figure 5.3. Subroutine *Waterdamage*.

The subroutine *SearchFP,* which has its flowchart represented in Figure 5.4, is called at every integration point, for each increment, to calculate the angle of the fracture plane θ_{fp}. Initially, the resistance of the action plane to transverse shear stressing $R^{A}_{\perp\perp}$ is calculated with equation (2.24). Then, with Equations (2.8)-(2.11) the stresses of the action plane can be obtained and then, if $\sigma_n > 0$ the local stress exposure f_e is calculated with equation (2.26) or if $\sigma_n < 0$ f_e is calculated with Equation (2.27). After those calculations, if f_e is higher than M[9], the angle associated with that calculation is saved. The cycle repeats until I=90.

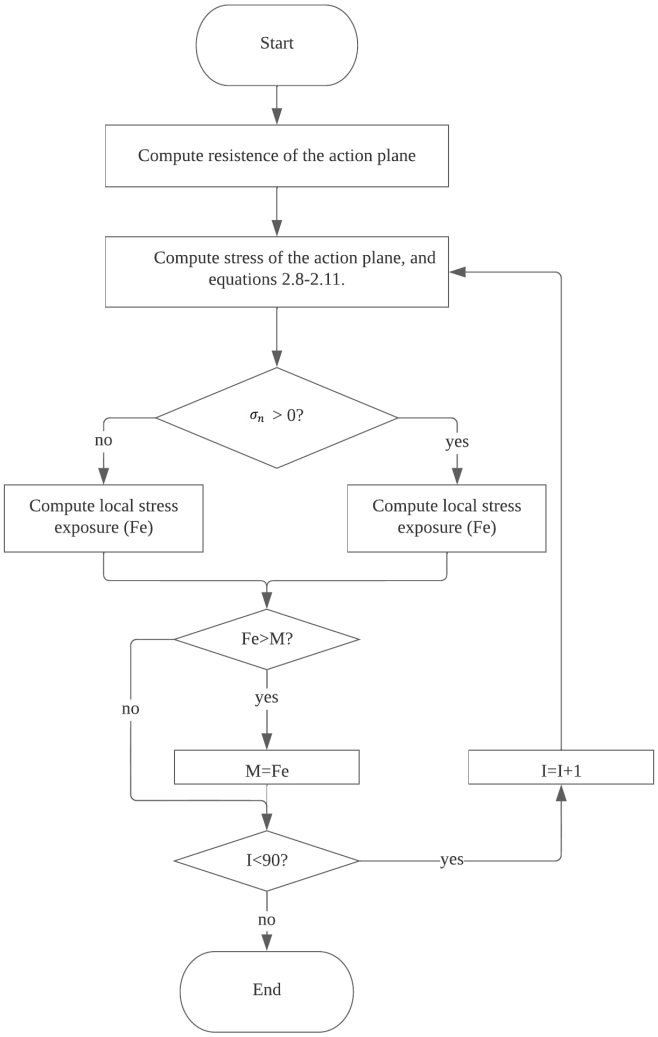

Figure 5.4. Subroutine SearchFP.

[9] Initially 0.

APPENDIX C- WET VOLUME FUNCTION

This appendix explains how the wet volume function was developed. For now, the concentration gradient is irrelevant; only the volume of water reached by water particles matters. The first term of Equation (5.1) concerns the wet volume induced by the diffusion process through surfaces D1, D2, C1, and C2. The second term accounts for the wet volume caused by the diffusion on surface A. The third term removes the intersection volume of the diffusion coming from surfaces D1 D2, and A.

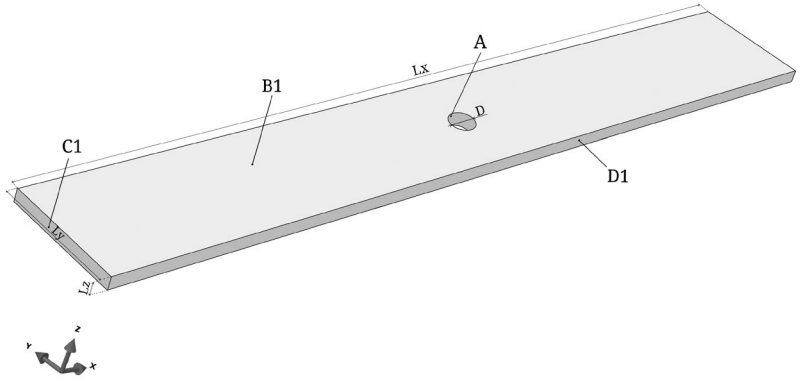

Figure 5.5. Identification of the specimen's surfaces and dimensions.

$$W_{volume}(D_{dist}) = 2L_z\, D_{dist}\{(L_y - 2D_{dist}) + (L_x)\} + L_z\pi\left(D_{dist} + \frac{D}{2}\right)^2 - L_z\pi\left(\frac{D}{2}\right)^2 - 4L_z \int_0^{\sqrt{-{L_Y}^2/4+4D_{dist}+D^2}} \int_{L_Y/2-D_{dist}}^{\sqrt{(D+D_{dist})^2-x^2}} dydx \quad (5.1)$$

This last complex double integral term can be avoided. The intersection between the diffusion of the surfaces D1, D2 and A only occurs when $D_{dist} = (L_z/2)/2 \approx 4.38\, mm$ since the diffusion process was considered equal in all surfaces. Furthermore, I_{vol} :

$$I_{vol} = \pi \left(\frac{L_Y}{2}\right)^2 L_z$$

Which is the volume of a cylinder with $r = \frac{L_Y}{2}$. The reason for the chosen distance to be $\frac{L_Y}{2}$ is the fact that, if the diffusion is equal in all surfaces, then then the diffusion will firstly cover all the specimen when $D_{dist} = \frac{L_Y}{2}$.

To replace the double integral of the Equation (5.1) a formulation requiring the following is needed:

- varies between 0 and 1
- only has a significant value when $D_{dist} \geq 4.38$
- is 1 if $D_{dist} = (L_z/2)$

The following equation fulfill all these requirements as Figure 5.6 depicts.

$$\mathrm{H}(D_{dist}) = Sin\left[\frac{\pi}{2}\left(\frac{D_{dist}}{L_z/2}\right)^5\right] \tag{5.2}$$

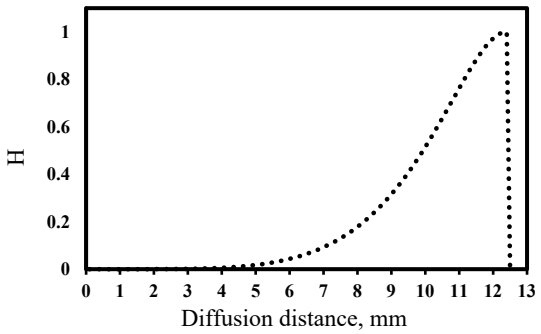

Figure 5.6. Variation of function $\mathbf{H}(\boldsymbol{D_{dist}})$.

And so, can be applied to replace the double integral term in conjunction with I_{vol}:

$$4L_z \int_0^{\sqrt{-L_Y{}^2/4+4D_{dist}+D^2}} \int_{L_Y/2-D_{dist}}^{\sqrt{(D+D_{dist})^2-x^2}} dydx \approx Sin\left[\frac{\pi}{2}\left(\frac{D_{dist}}{L_z/2}\right)^5\right] I_{vol} \tag{5.3}$$

$$\begin{aligned} W_{volume}(D_{dist}) &= 2L_z\, D_{dist}\{(L_y - 2D_{dist}) + (L_x)\} + L_z\pi\left(D_{dist} + \frac{D}{2}\right)^2 - L_z\pi\left(\frac{D}{2}\right)^2 \\ &\quad - Sin\left[\frac{\pi}{2}\left(\frac{D_{dist}}{L_z/2}\right)^5\right] I_{vol} \end{aligned} \tag{5.4}$$

APPENDIX D- DEVELOPED USER SUB-ROUTINE (UMAT)

```
      SUBROUTINE UMAT(STRESS,STATEV,DDSDDE,SSE,SPD,SCD,
     1 RPL,DDSDDT,DRPLDE,DRPLDT,
     2 STRAN,DSTRAN,TIME,DTIME,TEMP,DTEMP,PREDEF,DPRED,CMNAME,
     3 NDI,NSHR,NTENS,NSTATEV,PROPS,NPROPS,COORDS,DROT,PNEWDT,
     4 CELENT,DFGRD0,DFGRD1,NOEL,NPT,LAYER,KSPT,KSTEP,KINC)

      INCLUDE 'ABA_PARAM.INC'

      INTEGER
     1 I,J

      CHARACTER*80 CMNAME
      CHARACTER*80 CPNAME
      DIMENSION STRESS(NTENS),STATEV(NSTATEV),
     1 DDSDDE(NTENS,NTENS),DDSDDT(NTENS),DRPLDE(NTENS),
     2 STRAN(NTENS),DSTRAN(NTENS),TIME(2),PREDEF(1),DPRED(1),
     3 PROPS(NPROPS),COORDS(3),DROT(3,3),DFGRD0(3,3),DFGRD1(3,3)
      DOUBLE PRECISION
     1 E1,E2,E3,G12,G13,G23,V12,V13,V23,V21,V31,V32,SinPsi,ST(NTENS),
     2 XT,XC,YT,YC,FiberVolume,EF1,S21,FeFFT,FeFFTC,FeIFFT,FeIFFC,CosPsi,
     3 DMGFIBERT,DMGFIBERC,DMGMATRIXT,DMGMATRIXC,STRANT(NTENS),CD(NTENS,NTENS),DEGPROPS,
     4 FRAPTT,ZERO,ONE,MAXIM,MC(NTENS,NTENS),DF,DM,DELTA,ID,DIF,At
     5 Loop,Eq1,SigmaN,TaunT,TaunL,Theta,PI,FE,Eq2,MAXT,R,D,XX,YY,ZZ,CONC5,ti
     6 X1,X2,Y1,Y2,Z1,Z2,NFL,T,SWDMG,H,M00,MAXID,CONC,CONC1,CONC2,CONC3,CONC4,IncYM,YMPC

      INTEGER NTENS
      PARAMETER (ZERO=0.D0, ONE=1.D0)

      FiberVolume=PROPS(1)  !Major poisson's ratio fiber
      G12=PROPS(4)          !In plane shear modulus (12)
      V12=PROPS(5)          !Major Poisson's ratio (13)
      V23=PROPS(6)          !Through-thickness Poisson's ratio (23)
      EF1=PROPS(7)          !Fiber's Young's modulus in fiber's direction
      S21=PROPS(12)         !In plane shear strength
      ID=PROPS(13)          !Immersion days
      DEGPROPS=PROPS(14)    !Experimental fitting parameter
      IncYM=Props(15)        !Experimental fitting parameter
      YMPC=Props(16)        !Experimental fitting parameter
      G13=G12
      V13=V12               !Major Through-thickness Poisson's ratio (13)
```

```
      PI=3.1416
      DMGFIBERT=STATEV(1)      !Fiber damage due to tension
      DMGFIBERC=STATEV(2)      !Fiber damage due to compression
      DMGMATRIXT=STATEV(3)     !Matrix damage due to tension
      DMGMATRIXC=STATEV(4)     !Matrix damage due to compression
      Loop=ONE
      XT=STATEV(12)     !Tensile strength in fiber's direction
      XC=STATEV(13)     !Compressive strength in fiber's direction
      YT=STATEV(14)     !Tensile strength perpendicular to the fiber's direction
      YC=STATEV(15)    !Compressive strength perpendicular to the fiber's direction
      CONC=STATEV(11)
      ti=0.01

      T=ID*3600*24
      !Fick's law parameters
      DIF=0.000000018828
      H=2.3
      M00=1.04
      NFL=M00*(1-EXP(-7.3*(DIF*T/5.29)**0.75))/0.97583


       IF (Time(2).LE.ti) THEN
         MAXID=900
         ! Coordinates of the integration point
         XX=COORDS(1)
         YY=COORDS(2)
         ZZ=COORDS(3)
         M00=1.04
         !Normalized Fick's Law
         NFL=M00*(1-EXP(-7.3*(DIF*T/5.29)**0.75))/0.97583
         At=NFL+0.5*((1/(10**12)*ID**4)-((3/(10**9))*ID**3)+((3/(10**6))*ID**2)-((9/(10**4))*ID)-
1        0.0361)
         if (ID.GE.MAXID) then
           NFL=1
         end if
          Ddist=At*0.01125
         !Diffusion distance to origin
         X1=-0.085+ Ddist        !Surface C1
         X2=0.085- Ddist         !Surface C2
         Y1=-0.01125+ Ddist      !Surface D1
         Y2=0.01125- Ddist       !Surface D2
         R=SQRT(XX*XX+YY*YY)
         D=0.0025+ Ddist         !Surface A
         SWDMG=0
           !verification: is the integration point in the damaged zone?
         if (R.LE.D.OR.XX.LE.X1.OR.XX.GE.X2.OR.YY.LE.Y1.OR.YY.GE.Y2) then
```

```
      !Concentration of seawater
      if (XX.GE.X2) then
         CONC1=1-ABS((0.0825-XX)/( Ddist))
      end if
      if (XX.LE.X1) then
         CONC2=1-ABS((-0.0825-XX)/( Ddist))
      end if
      if (YY.LE.Y1) then
         CONC3=1-ABS((-0.01125-YY)/( Ddist))
      end if
      if (YY.GE.Y2) then
         CONC4=1-ABS((0.01125-YY)/( Ddist))
      end if
      if (R.LE.D) then
         CONC5=1-ABS((R-0.0025)/( Ddist))
      end if
      CONC=MAX(CONC1,CONC2,CONC3,CONC4,CONC5)
      SWDMG=1
      STATEV(10)=SWDMG
      STATEV(11)=CONC
      XT=PROPS(8)*(1-DEGPROPS*CONC)
      XC=PROPS(9)*(1-DEGPROPS*CONC)
      YT=PROPS(10)*(1-DEGPROPS*CONC)
      YC=PROPS(11)*(1-DEGPROPS*CONC)
   else
         XT=PROPS(8)
         XC=PROPS(9)
         YT=PROPS(10)
         YC=PROPS(11)
         CONC=0
         STATEV(11)=CONC
         STATEV(12)=XT
         STATEV(13)=XC
         STATEV(14)=YT
         STATEV(15)=YC
   end if
    STATEV(12)=XT
    STATEV(13)=XC
    STATEV(14)=YT
    STATEV(15)=YC
end if

E1=Props(2)*IncYM+Props(2)*NFL*(YMPC)
E2=Props(3)*IncYM+Props(3)*NFL*(YMPC)
E3=E2
V21=(E2/E1)*V12
```

```
        V31=(E3/E1)*V13
        V32=(E3/E2)*V23
        G23=E2/2/(1.+V23)

        !Strain
      do I = 1, NTENS
         STRANT(I) = STRAN(I) + DSTRAN(I)
      enddo

        !Compute constitutive matrix and stress state
      callCONSTITUTIVE(MC,E1,E2,E3,G12,G13,G23,V12,V13,V23,V21,V31,V32,NTENS,DMGFIBERT,DMGFIBERC,DM
GMATRIXT,DMGMATRIXC)
      do i=1,NTENS
          ST(i)=0.0D0
          do j=1,NTENS
              ST(i)=ST(i)+MC(j,i)*STRANT(j)
          enddo
      enddo
      STRESS=ST
      DDSDDE=MC

      do while ( Loop.EQ.ONE )
          callCONSTITUTIVE(MC,E1,E2,E3,G12,G13,G23,V12,V13,V23,V21,V31,V32,NTENS,DMGFIBERT,DMGFIBER
C,DMGMATRIXT,DMGMATRIXC)
          do i=1,NTENS
              ST(i)=0.0D0
              do j=1,NTENS
                  ST(i)=ST(i)+MC(j,i)*STRANT(j)
              enddo
          enddo
            FRAPTT = (S21/(2*0.23))*(sqrt((1+2*0.23*YC/S21))-1) !fracture resistance of the action
plane
          do I = -90,90
            Theta = I*PI/180
              SigmaN=ST(2)*(COS(Theta))**2+ST(3)*(SIN(Theta))**2+2*(ST(6)/2)*SIN(Theta)*COS(Theta)
              TaunT=-ST(2)*SIN(Theta)*COS(Theta)+ST(3)*SIN(Theta)*COS(Theta)+
                (ST(6)/2)*((COS(Theta))**2-(SIN(Theta))**2)
              TaunL=(ST(5)/2)*SIN(Theta)+(ST(4)/2)*COS(Theta)
              CosPsi=TaunT**2/(TaunT**2+TaunL**2)
              SinPsi=TaunL**2/(TaunT**2+TaunL**2)
              Eq1=(0.23/FRAPTT)*CosPsi+(0.3/S21)*SinPsi
              Eq2=(0.23/FRAPTT)*CosPsi+(0.25/S21)*SinPsi
              if(SigmaN.GE.ZERO) then
                  FE =SQRT((((1/YT)-Eq1)*SigmaN)**2+(TaunT/FRAPTT)**2+(TaunL/S21)**2)+Eq1*SigmaN
              else
                  FE = SQRT((TaunT/FRAPTT)**2+(TaunL/S21)**2+(Eq2*SigmaN)**2)+Eq2*SigmaN
```

```
            end if
            if(FE.GT.MAXIM) then
                MAXIM=FE
                MAXT=Theta
            end if
         enddo
         Theta=MAXT

!.........................Puck's failure criterion.....................................

        if((ST(1)-(V12-FiberVolume*1.3*E1/EF1)*(ST(2)+ST(3))).GE.ZERO) then
            !Local stress exposure: Fiber under tension
            FeFFT=(ST(1)-(V12-FiberVolume*1.3*E1/EF1)*(ST(2)+ST(3)))/XT
            FeFFTC= ZERO
            if (FeFFT.GE.ONE) then
                Loop=ONE
            end if
         else
           !Local stress exposure: Fiber under compression
            FeFFTC = ABS((ST(1)-(V12-FiberVolume*1.3*E1/EF1)*(ST(2)+ST(3))))/XC
            FeFFT = ZERO
            if (FeFFTC.GE.ONE) then
                Loop=ONE
            end if
         end if

           FRAPTT = (S21/(2*0.25))*(sqrt((1+2*0.25*YC/S21))-1)
           SigmaN=ST(2)*(COS(Theta))**2+ST(3)*(SIN(Theta))**2+2*(ST(6)/2)*SIN(Theta)*COS(Theta)
           TaunT=-ST(2)*SIN(Theta)*COS(Theta)+ST(3)*SIN(Theta)*COS(Theta)+
           (ST(6)/2)*((COS(Theta))**2-(SIN(Theta))**2)
           TaunL=(ST(5)/2)*SIN(Theta)+(ST(4)/2)*COS(Theta)
           CosPsi=TaunT**2/(TaunT**2+TaunL**2)
           SinPsi=TaunL**2/(TaunT**2+TaunL**2)
           Eq1=(0.23/FRAPTT)*CosPsi+(0.3/S21)*SinPsi
           Eq2=(0.23/FRAPTT)*CosPsi+(0.25/S21)*SinPsi

          !Local stress exposure: Matrix under tension
         if(SigmaN.GE.ZERO) then
            FeIFFT=SQRT((((1/YT)-Eq1)*SigmaN)**2+(TaunT/FRAPTT)**2+(TaunL/S21)**2)+Eq1*SigmaN
            FeIFFC=ZERO
         end if
          !Local stress exposure: Matrix under compression
         if(SigmaN.LT.ZERO) then
            FeIFFC=SQRT((TaunT/FRAPTT)**2+(TaunL/S21)**2+(Eq2*SigmaN)**2)+Eq2*SigmaN
            FeIFFT=ZERO
         end if
```

```
      if (FeIFFC.GE.ONE.OR.FeIFFT.GE.ONE.OR.FeFFT.GE.ONE.OR.FeFFTC.GE.ONE) then
          Loop=ONE
      else
          Loop=ZERO
      end if

      if(DMGFIBERT.GE.1) FeFFT=1
      if(DMGFIBERC.GE.1) FeFFTC=1
      if(DMGMATRIXT.GE.1) FeIFFT=1
      if(DMGMATRIXC.GE.1) FeIFFC=1
      if(FeFFT.LE.ONE.AND.FeFFTC.LE.ONE.AND.FeIFFT.LE.ONE.AND.FeIFFC.LE.ONE) then
          Loop=ZERO
      end if

        !Degradation

      if(FeFFT.GT.ONE) THEN
          DMGFIBERT=1
      end if
      if(FeFFTC.GT.ONE) THEN
          DMGFIBERC=1
      end if
      if(FeIFFT.GT.ONE.AND.DMGMATRIXT.EQ.ZERO) THEN
          DMGMATRIXT=1
      end if
      if(FeIFFC.GT.ONE.AND.DMGMATRIXC.EQ.ZERO) THEN
          DMGMATRIXC=1
      end if
  enddo
  Theta=Theta*180/(PI)

    !State variables
  STATEV(1)=DMGFIBERT
  STATEV(2)=DMGFIBERC
  STATEV(3)=DMGMATRIXT
  STATEV(4)=DMGMATRIXC
  STATEV(5)=Theta
  STATEV(6)=FeFFT
  STATEV(7)=FeFFTC
  STATEV(8)=FeIFFT
  STATEV(9)=FeIFFC
  return
  end
```

```
      SUBROUTINECONSTITUTIVE(MC,E1,E2,E3,G12,G13,G23,V12,V13,V23,V21,V31,V32,NTENS,DMGFIBERT,DMGFIB
ERC,DMGMATRIXT,DMGMATRIXC)
        include 'ABA_PARAM.INC'
        INTEGER NTENS
        DOUBLE PRECISION MC(NTENS,NTENS)
        PARAMETER (ZERO=0.D0, ONE=1.D0)

        do i=1,NTENS
          do j=1,NTENS
              MC(i,j)=0.D0
          enddo
        enddo

        DF=1-(1-DMGFIBERT)*(1-DMGFIBERC)
        DM=1-(1-DMGMATRIXT)*(1-DMGMATRIXC)
        DELTA=1/(1-V12*V21-V23*V32-V13*V31-2*V21*V32*V13)
        MC(1,1)=(1-DF)*E1*(1-V23*V32)*DELTA
        MC(1,2)=(1-DF)*(1-DM)*E1*(V21+V31*V23)*DELTA
        MC(1,3)=(1-DF)*(1-DM)*E1*(V31+V21*V32)*DELTA
        MC(2,1)=MC(1,2)
        MC(2,2)=(1-DF)*(1-DM)*E2*(1-V13*V31)*DELTA
        MC(2,3)=(1-DF)*(1-DM)*E2*(V32+V12*V31)*DELTA
        MC(3,1)=MC(1,3)
        MC(3,2)=MC(2,3)
        MC(3,3)=(1-DF)*(1-DM)*E3*(1-V12*V21)*DELTA
        MC(4,4)=(1-DF)*(1-0.9*DMGMATRIXT)*(1-0.5*DMGMATRIXC)*G12
        MC(5,5)=(1-DF)*(1-0.9*DMGMATRIXT)*(1-0.5*DMGMATRIXC)*G13
        MC(6,6)=(1-DF)*(1-0.9*DMGMATRIXT)*(1-0.5*DMGMATRIXC)*G23

        return
        end
```